Remote Sensing of Environment 237 (2020) 111540

Contents lists available at ScienceDirect

Remote Sensing of Environment

journal homepage: www.elsevier.com/locate/rse

# A semi-empirical method for estimating complete surface temperature from radiometric surface temperature, a study in Hong Kong city

Jinxin Yang[a], Man Sing Wong[b,*], Hung Chak Ho[b,c], E. Scott Krayenhoff[d], P.W. Chan[e], Sawaid Abbas[b], Massimo Menenti[f,g]

[a] School of Geographical Science, Guangzhou University, Guangzhou 510275, PR China
[b] Department of Land Surveying and Geo-Informatics, The Hong Kong Polytechnic University, Kowloon, Hong Kong, PR China
[c] Department of Urban Planning and Design, The University of Hong Kong, Hong Kong, PR China
[d] School of Environmental Sciences, University of Guelph, Guelph, ON, Canada
[e] Hong Kong Observatory, Hong Kong, PR China
[f] Faculty of Civil Engineering and Earth Sciences, Delft University of Technology, P. O. Box 5048, 2600 GA Delft, Netherlands
[g] State Key Laboratory of Remote Sensing Science, Institute of Remote Sensing and Digital Earth, Chinese Academy of Sciences, Beijing 100101, PR China

ARTICLE INFO

*Keywords:*
Remote sensing
Surface temperature
Thermal heterogeneity
Urban geometry

ABSTRACT

The complete surface temperature ($T_c$) in urban areas, defined as the mean temperature of the total active surface area, is an important variable in urban micro-climate research, specifically for assessment of the urban surface energy balance. Since most vertically-oriented building facets are not observed by a nadir-viewing remote imaging radiometer, the radiometric surface temperature ($T_r$) measured at a specific view angle cannot be used with existing heat transfer equations to estimate radiative and convective fluxes in the urban environment. Thus, it is necessary to derive $T_c$ for city neighborhoods. This study develops a simple method to estimate $T_c$ from $T_r$ with the aid of the Temperatures of Urban Facets in 3D (TUF-3D) numerical model, which calculates 3-D sub-facet scale urban surface temperatures for a variety of surface geometries and properties, weather conditions and solar angles. The effects of geometric and meteorological characteristics – e.g., building planar area index ($\lambda_p$), wall facet area index ($F$), solar irradiance – on the difference between $T_c$ and $T_r$ were evaluated using the TUF-3D model. Results showed the effects of geometric and meteorological characteristics on the difference between $T_c$ and $T_r$ differ between daytime and nighttime. The study then sought to predict the relationship between $T_r$ and $T_c$, using $\lambda_p$, $F$, and solar irradiance for daytime and only using $\lambda_p$ and $F$ for nighttime. Based on the simulated data from TUF-3D, the resulting relationships achieve a coefficient of determination ($r^2$) of 0.97 and a RMSE of 1.5 K during daytime, with corresponding nighttime values of $r^2 = 0.98$ and RMSE = 0.69 K. The relationships between $T_r$ and $T_c$ are evaluated using high resolution airborne thermal images of daytime urban scenes: $r^2 = 0.75$ and RMSE = 1.09 K on August 6, 2013 at 12:40 pm; and $r^2 = 0.86$ and RMSE = 1.86K on October 24, 2017 at 11:30 am. The new relationships were also applied to estimate $T_c$ from $T_r$ in Hong Kong retrieved from Landsat 5 Thematic Mapper (TM) and the Advanced Spaceborne Thermal Emission and Reflection Radiometer (ASTER). In the present climatic context, the difference between $T_c$ and $T_r$ can reach 10 K during daytime in summer, and 6 K during daytime in winter, with seasonal variation attributable to the variations in shortwave irradiance. The nighttime difference between $T_c$ and $T_r$ can also reach 2 K in both summer and spring seasons.

*Abbreviations:* $T_c$, complete surface temperature (K); $T_r$, radiometric temperature from nadir view direction (K); TUF-3D, Temperatures of Urban Facets in 3D; $\lambda_p$, planar area index; F, wall facet area index; ASTER, Advanced Spaceborne Thermal Emission and Reflection Radiometer; TM, Landsat thematic mapper; UST, urban surface temperature (K); LASER/F, LAtent, SEnsible, Radiation Fluxes; $Kn$, solar radiation above urban canopy (W/m$^2$); $\theta_a$, solar azimuth angle (°); $\theta_z$, solar zenith angle (°); $T_{roof}$, roof temperature (K); $T_{road}$, road temperature (K); $T_{wall}$, wall temperature (K); $L_r$, radiation at the bottom of atmosphere at nadir view modelled by TUF-3D (W/m$^2$); ε, emissivity; σ, Stefan–Boltzmann constant ($5.6703 \times 10^{-8}$ Wm$^{-2}$ K$^{-4}$); $L_d$, downwelling atmospheric radiation; $E(i)$, radiance leaving urban canopy of pixel $i$ (W·m$^{-2}$·sr$^{-1}$·μm$^{-1}$); $R_{at\uparrow}$, downward atmospheric thermal radiance (W·m$^{-2}$·sr$^{-1}$·μm$^{-1}$)

* Corresponding author.
*E-mail addresses:* yangjx11@gzhu.edu.cn (J. Yang), lswong@polyu.edu.hk (M.S. Wong), hcho21@hku.hk (H.C. Ho), skrayenh@uoguelph.ca (E.S. Krayenhoff), pwchan@hko.gov.hk (P.W. Chan), m.menenti@tudelft.nl (M. Menenti).

https://doi.org/10.1016/j.rse.2019.111540
Received 8 April 2018; Received in revised form 8 October 2019; Accepted 11 November 2019
0034-4257/ © 2019 Elsevier Inc. All rights reserved.

## 1. Introduction

### 1.1. Background

Urban Surface Temperature (UST) is a key variable for studying urban surface energy exchange and microclimate in an urban environment (Arnfield, 2003; Arnfield and Grimmond, 1998; Cheng et al., 2010; Morrison et al., 2018; Nazarian et al., 2018a; Oke, 1988; Voogt and Oke, 2003; Yaghoobian et al., 2010). Satellite-based thermal infrared (TIR) data have been used for studying urban surface temperature and provide information at different temporal and spatial scales (Li et al., 2013), thus surface temperature from remote sensing data has been widely applied in urban climate research (Dousset and Gourmelon, 2003; Roth et al., 1989; Voogt and Oke, 2003; Weng, 2009). Most space-borne imaging radiometers observe terrestrial targets in a close to nadir view direction and, therefore, can capture only horizontal facets. Thus, active radiation sources would be incompletely observed over urban areas (Adderley et al., 2015; Jiang et al., 2018; Roth et al., 1989). Theoretically, off-nadir-view satellite sensors can observe the vertical walls, but only a few multi-angle sensors provide off-nadir image data with thermal infrared spectral range, and such satellite images (e.g. Sea and Land Surface Temperature Radiometer (SLSTR) on-board Sentinel 3, ATSR-series) are with low spatial resolution (1 km), which is not capable to be used over high-density urban environment. For densely built areas, active radiation sources are much larger than the horizontal area due to the large surface area of vertical facets (Roth et al., 1989). It is therefore challenging to retrieve urban surface temperature accurately and without large bias using thermal infrared remote sensing (Jiang et al., 2018).

In terms of the urban energy balance, convective heat transfer is often influenced by the complete surface of each roughness element. Thus, a representative surface temperature of the complete and 3D surface-atmosphere interface should be estimated since these temperatures contribute to the local heat exchange (Kanda et al., 2007; Kanda et al., 2005; Voogt and Oke, 1997). Voogt and Oke (1997) proposed the concept of the complete urban surface temperature ($T_c$), defined as weighted summation of the component surface temperatures, multiplied by the associated component fractions from a three-dimensional perspective. Compared with the radiometric surface temperature directly captured by a nadir-viewing remote imaging radiometer, $T_c$ can provide superior information towards understanding urban climate. Voogt and Oke (1997) compared sensible heat fluxes calculated from air temperature and different surface temperatures, and their results showed that the complete surface temperature should be used for the estimation of sensible heat flux in urban areas. In order to consider its significant implications in urban climate research, researchers have attempted to calculate $T_c$ from remote sensing or field measurements (Allen et al., 2018; Jiang et al., 2018; Voogt and Oke, 1997). Voogt and Oke (1997) calculated $T_c$ based on field measurement by a thermal camera data and digitizing building data from high-resolution (1:2500) aerial photography. Their results showed that there is a significant difference between $T_c$ and the nadir $T_r$. Allen et al. (2018) calculated $T_c$ from the hemispherical $T_r$ measured by pyrgeometers and results showed that the difference between $T_c$ and the temperature observed from a nadir view is up to 8 K under clear-sky viewing conditions. Jiang et al. (2018) estimated $T_c$ from directional radiometric temperature based on simulated data from urban micro-climate model and remote sensing observation model, without ancillary ground-based data. They indicated that the estimation of $T_c$ could be further improved by using radiometric temperatures observed at multiple view-angles.

### 1.2. Gaps in knowledge

The aforementioned studies estimated the $T_c$ using field measurements or airborne data, while the estimation of $T_c$ from satellite remote sensing data is still challenging due to their relatively low spatial resolution and to the thermal heterogeneity within the mixed pixels, which include roof and road facets with different temperatures. Since radiometric temperature is more readily available from satellite images than $T_c$, this study proposes a simple method to estimate $T_c$ from nadir observations of radiometric temperature view ($T_r$). A nadir viewing imaging radiometer can only observe the radiance emitted by horizontal facets and reflected by horizontal facets from facets around and atmosphere. The temperature of horizontal facets is also affected by vertical walls due to the radiative transfer and energy exchange between vertical walls and road surfaces (Nazarian and Kleissl, 2015; Yang and Li, 2015). Thus, $T_r$ is related to wall temperatures and related to $T_c$ to some extent. $T_r$ and $T_c$ are correlated with the building height, density of building, material and local climatic conditions. Buildings in a city have influences on the radiative and convective transfer and imply energy exchange of the wall facets with ambient atmosphere, which results in the spatial variability of urban surface temperature. In addition, shadows cast by buildings affect the variability of surface temperatures. For homogeneous or “pure” pixels, $T_r$ and $T_c$ are more or less identical, while thermally heterogeneous pixels in urban spaces are always affected by the complexity of urban surfaces, including building density, aspect ratio (ratio of building height to the street width), and material properties which contribute differently to energy exchange. Thus, the relationships between $T_r$ and $T_c$ can be parameterized by urban structural parameters (e.g. building density, building height) and local meteorological parameters. In order to develop the relationships, complex energy exchange within mixed pixels with high heterogeneity of urban surface temperature should be modelled.

The Temperatures of Urban Facets in 3D (TUF-3D) numerical model was adopted and used in this study to simulate $T_r$ and $T_c$ (Krayenhoff and Voogt, 2007). TUF-3D provides (sub-) facet surface temperatures based on sub-facet scale solutions to the surface energy balance. The $T_c$ can also be calculated therefore, by combining the facet surface temperatures provided by TUF-3D with the associated facet areas. $T_r$ is provided by TUF-3D in order to represent a sensor viewing from a nadir direction, and it is calculated from the radiation emitted and reflected by roofs and roads.

### 1.3. Objectives

In order to estimate $T_c$ from $T_r$, this study explored and established a relationship between $T_c$ and $T_r$ in a thermally heterogeneous environment with the use of numerical experiments based on TUF-3D and urban building structure parameters (Planar Area Index ($\lambda_p$) and Wall Facet area index ($F$). The objectives of this study were 1) to assess the effects of urban building geometric parameters (e.g. $\lambda_p$, $F$) and local meteorological conditions (e.g. wind speed, solar radiation) on the relationship between $T_c$ and $T_r$; and 2) to evaluate the relationship between $T_c$ and $T_r$ using an urban energy balance model and numerical experiments and develop a simple method that uses $T_r$ to retrieve $T_c$ in a thermally heterogeneous urban environment. Subsequently, the developed method is used to estimate $T_c$ from radiometric surface temperature observed by satellite data of the Landsat 5 Thematic Mapper (TM) with 30 m spatial resolution in daytime and Advanced Spaceborne Thermal Emission and Reflection Radiometer (ASTER) with 90 m spatial resolution in nighttime.

The study is organized as follows. After an Introduction structured in two sub-sections to articulate our problem statement, the objectives are stated, followed by a detailed presentation of the Methodology structured in five sub–sections, to describe separately a sensitivity analysis and the design of numerical experiments from the development of a simple model to estimate $T_c$ from $T_r$. Next, the data applied in the study are described by type, i.e. radiometric data acquired by satellites, digital surface models and meteorological data. The presentation of results mirrors the structure of the Methodology and is followed by a detailed Discussion. Lastly, the section of Conclusions is presented.

## 2. Methodology

### 2.1. General

In this study, a simple method is developed to estimate the complete surface temperature $T_c$ from remote sensing measurements of the radiometric surface temperature $T_r$ for daytime and nighttime respectively. For daytime, the method is based on a relationship $f_d$:

$$T_c = f_d(T_r, \lambda_p, F, Kn, \theta_a, \theta_z) \quad (1)$$

where $T_r$ is the nadir radiometric temperature (K), $\lambda_p$ is the planar area index, $F$ is the wall facet area index, $Kn$ is the down-welling solar irradiance at the top of the urban canopy ($W/m^2$), $\theta_a$ is the solar azimuth angle (°), and $\theta_z$ is the solar zenith angle (°). $\lambda_p$, defined as the ratio of plan area of buildings to the area of building footprint, is related to the building density. Specifically, $\lambda_p$ is defined as the ratio of building total planar area to the area of the horizontal plane section of the building at ground level. The building footprint is the area of the horizontal plane section of the building at ground level. The wall facet area index ($F$), calculated as the ratio of the wall facet area to the area of building footprint which contains the building and the road around it, is related to the building density and aspect ratio. $\lambda_p$ is related to the directional temperature observed by remote sensing from nadir direction. $F$ is related to the fraction unobserved by remote sensing. Thus, $F$ and $\lambda_p$ were used in this study as the building structure parameters to study the difference between $T_c$ and $T_r$.

Fewer variables and parameters are taken into account during nighttime since the solar effects can be neglected at nighttime and the relationship between $T_c$ and $T_r$ becomes:

$$T_c = f_n(T_r, \lambda_p, F) \quad (2)$$

To construct our simple model, we used a large number of numerical experiments (see Section 2.3 for details) by TUF 3D (Krayenhoff and Voogt, 2007) to generate the pseudo – observations required to determine the relationships Eq. (1) and (2). Considering that the solar effects would continue about 3 h after sunset, the daytime numerical experiments from 8:00 am until 5:00 pm and the nighttime numerical experiments from 9:00 pm until 5:00 am were used for studying the relationships in Eqs. (1) and (2) between $T_c$ and $T_r$.

Our study was limited to the built-up area where the fractional abundance of vegetation is negligible, so that the temperature of vegetation is not considered in this study. This is also aligned with our estimation in the TUF-3D model. The $T_c$ was calculated using the facet temperatures (roof temperature $T_{roof}$, road temperature $T_{road}$ and wall temperature $T_{wall}$) and the facet area weights extracted from the TUF-3D output:

$$T_c = \frac{T_{roof} * \lambda_p + T_{road} * (1 - \lambda_p) + T_{wall} * F}{1 + F} \quad (3)$$

$T_r$ was calculated from the area-weighted average of upwelling radiation from roof and road facets according to the definition given by Becker and Li (1995). Since satellite sensors have narrow fields of view, only the roof and road facets are observed from a nadir view. The upwelling radiation includes the emitted radiation by roof and road facet and the radiation emitted by wall facets and atmosphere, then reflected by roof and road facets. The reflected radiation depends on the wall surface temperature and material emissivities of walls and roads as well as the sensor-ground geometry. In this study, we only consider the nadir radiometric temperature. In the TUF – 3D domain, we obtained the $T_r$ from the radiation at the bottom of atmosphere $L_r$ captured by the pseudo – observations collected by a fictive nadir – viewing imaging radiometer placed:

$$L_r = \varepsilon\sigma T_r^4 + (1 - \varepsilon)L_d \quad (4)$$

$\varepsilon$ is calculated as the area-weighted average of roof and road emissivities. σ is the Stefan–Boltzmann constant ($5.6703 \times 10^{-8}$ $Wm^{-2}$ $K^{-4}$). $L_d$ is the downwelling atmospheric radiation, $T_r$ is the radiometric temperature measured by a fictive nadir-viewing remote radiometerer. The TUF-3D provides the upwelling radiation from road and roof which includes the radiation emitted by roof and road facets and the radiation emitted by wall facets and by the atmosphere and reflected by roof and road facets. Then the $L_r$ can be calculated as the area weighted average of roof and road facets. $L_d$ is calculated from the atmospheric profile in TUF-3D.

The design of the numerical experiments is described in Section 2.3. The variables and parameters in the Eqs. (1) and (2) (e.g. $\lambda_p$, $F$, $Kn$, $\theta_a$, $\theta_z$) may have different influence on the relationship between $T_c$ and $T_r$. The approach to evaluate how influential such variables and parameters are, is explained in Section 2.4. Finally, the relationships in Eqs. (1) and (2) were determined and evaluated as described in Sections 2.5 and 2.6.

### 2.2. Overview of the TUF-3D model

TUF-3D is a micro-scale urban energy balance model that represents the three-dimensional (3D) energy exchange in response to meteorological forcing, i.e. solar irradiance, wind speed and air temperature. The energy fluxes and (sub-) facet surface temperatures calculated with this model have been validated with measurements (Krayenhoff and Voogt, 2007). TUF-3D has also been used to estimate UST of heterogeneous pixels from the facet surface temperatures (Krayenhoff and Voogt, 2016), as well as to evaluate radiation models (Krayenhoff et al., 2014). TUF-3D describes sensible heat transfer in a simplified way by assuming that a constant flux layer extends to the surface, wherein the vertical profiles of wind speed and temperature are logarithmic (Krayenhoff and Voogt, 2007). This assumption can reduce computational costs in view of modelling large neighborhood or entire cities. In reality, heat transfer is complex because of the coherent turbulent structures and the complexity of the urban canopy layer due to the complex urban morphology and heterogeneous urban facets(Grimmond et al., 2011; Grimmond et al., 2010; Wang et al., 2014).The hypothesis of logarithmic vertical profiles of wind speed and air temperature is widely adopted in urban micro-climate models, e.g. LASER/F (LAtent, SEnsible, Radiation Fluxes) (Kastendeuch and Najjar, 2009; Kastendeuch et al., 2017). Lee et al. (2013) applied LASER/F to generate synthetic, high-resolution thermal images of building facets and evaluated the impact of the simplified description of momentum and heat transfer in LASEF/F by comparing it with a Computational Fluid Dynamics (CFD) model. The results showed that the impact on facet energy balance and surface temperature was relatively small. Accordingly, we accepted the hypothesis of logarithmic profiles in the urban canopy layer in TUF-3D.

### 2.3. Design of numerical experiments

Urban geometric parameters, including building planar area index ($\lambda_p$) and aspect ratio, and local meteorological conditions, including wind speed and solar radiation, have a direct impact on the relationship between $T_c$ and $T_r$. To study the influence of these variables and parameters on the difference between $T_c$ and $T_r$, several numerical experiments for different values of $\lambda_p$ and aspect ratio under different meteorological conditions were carried out. The total number of numerical experiments is limited by available computational resources, so we limited the number of levels applied for each variable and parameter. According to Stewart et al. (2014), $\lambda_p$ ranges from 0.1 to 0.90 and aspect ratio ranges between 0.1 and > 2.5 for typical urban local climate zones. The $\lambda_p$ ranges from 0.1 to 0.70 in this study because of the computing ability. Aspect ratio is calculated as the ratio of building height to street width. In TUF-3D, $\lambda_p$ and ratio of building height to length (H/L) can be used to replace the aspect ratio. In the TUF-3D, a building has a square horizontal section. The building length is equal to the building width of the building roof or base. The meteorological

**Table 1**
Surface building geometries and dates of meteorological parameters used in TUF-3D.

| $\lambda_p$ | H/L | Dates of meteorological parameters (Solar radiation, wind speed, air temperature, air pressure) |
|---|---|---|
| 0.1–0.7 | 0.5–5.5 | Feb 27, 2010; Mar 10, 2010; Apr 11, 2010; May 25, 2010; Jul 1, 2010; Aug 2, 2010; Sept 17, 2010; Oct 28, 2010; Nov 27, 2010; Dec 7, 2010 |

**Table 2**
Thermal and radiative properties used in TUF-3D (Stewart et al., 2014).

| Surface properties | Group1 | Group 2 | Group 3 | Group 4 | Group 5 | Group 6 | Group 7 | Group 8 | Group 9 | 10 |
|---|---|---|---|---|---|---|---|---|---|---|
| Emissivity: | | | | | | | | | | |
| Roof | 0.937 | 0.945 | 0.937 | 0.945 | 0.937 | 0.945 | 0.937 | 0.945 | 0.937 | 0.945 |
| Wall | 0.956 | 0.886 | 0.956 | 0.886 | 0.956 | 0.886 | 0.956 | 0.886 | 0.956 | 0.886 |
| Ground | 0.956 | 0.948 | 0.956 | 0.948 | 0.956 | 0.948 | 0.956 | 0.948 | 0.956 | 0.948 |
| Albedo: | | | | | | | | | | |
| Roof | 0.13 | 0.18 | 0.15 | 0.13 | 0.13 | 0.13 | 0.13 | 0.18 | 0.13 | 0.1 |
| Wall | 0.25 | 0.2 | 0.2 | 0.25 | 0.25 | 0.2 | 0.2 | 0.25 | 0.25 | 0.2 |
| Ground | 0.15 | 0.16 | 0.18 | 0.2 | 0.2 | 0.24 | 0.24 | 0.17 | 0.23 | 0.21 |
| Thermal conductivity (W/m/K): | | | | | | | | | | |
| Roof | 1.4 | | | | | | | | | |
| Wall | 1.12 | | | | | | | | | |
| Ground | 0.84 | | | | | | | | | |
| Volumetric heat capacity ($10^6$J/m$^3$/K): | | | | | | | | | | |
| Roof | 1.61 | 1.61 | 1.02 | 1.60 | 1.60 | 1.02 | 2.85 | 1.60 | 1.03 | 2.85 |
| Wall | 1.75 | 3.57 | 2.28 | 2.58 | 2.58 | 2.28 | 0.32 | 2.01 | 2.29 | 2.01 |
| Ground | 1.59 | 1.45 | 1.33 | 1.17 | 1.10 | 1.04 | 0.84 | 1.42 | 0.89 | 1.08 |

data, including solar radiation, wind speed, air temperature, air pressure, on cloudless days of each month from the Hong Kong Observatory were selected as input (Table 1).

The values of thermal and radiative parameters of urban materials adopted in this study were also based on Stewart et al. (2014) and explore a broad range of conditions, so that the results of the analysis apply to a range of different urban conditions, e.g. from high-rise compacted city to open low-rise city space. The material properties in real world are complex, the values used in this study can represent the typical condition of the real world (Stewart et al., 2014). The material emissivity spectra of rooftop, wall facet and road were applied to estimate the emissivities in the Landsat 5 TM and ASTER spectral bands (Table 2). The material emissivity is calculated from the urban material spectral library (Kotthaus et al., 2014) and the satellite spectral response functions used in this study. We assume that roof is constructed by concrete and brick, and the material emissivity of roof is the average value of concrete and brick. The road is constructed by the concrete and asphalt and the material emissivity of road is the average value of concrete and asphalt.

The geometric and meteorological parameters in Table 1 were combined with thermal and radiative material properties in Table 2 to carry out the numerical experiments with TUF 3D. In total about 17,000 sets of data were carried out. Subsets of the results were used in the sensitivity analysis described in Section 2.4, while the results of all experiments were combined to determine our simple model (Section 2.5).

### 2.4. Evaluation of influential urban properties

Synthetic data on $T_c$ and $T_r$ were generated with TUF-3D and used as pseudo-observations to construct relationships between $T_c$ and $T_r$ (see Section 2.5). Prior to that, we have evaluated the influence of urban properties on the relation between $T_c$ and $T_r$ as described in this section.

The urban geometric parameters, $\lambda_p$ and $F$, were used to represent the urban geometric characteristics and further study the relationship between $T_r$ and $T_c$. The wind speed ($w$) in TUF-3D is set at above canopy height, estimated as twice the building height. Wind has different effects on roof and ground surface temperature and these effects depend on building density and aspect ratio (Nazarian and Kleissl, 2015). Daytime $T_c$ can be written as a function of $T_r$, urban geometry, solar irradiance and solar position. The sensitivity of $T_c$ to urban variables and parameters was evaluated by determining several different regressions, as listed in Table 3. The sensitivity analysis in Table 3 determines how the different variables affect the difference between $T_c$ and $T_r$ and which kind of equations should be constructed to estimate $T_c$.

**Table 3**
Sensitivity analysis of Eq. (1). (The column of "specific sensitivity" describes each component of the sensitivity analysis by listing first the independent variables, then the variables taken as dependent; the column of "variables" lists the variables involved in the component sensitivity analysis; the column of "purposes" explains the objective of each component sensitivity analysis).

| Specific sensitivity | Variables | Purposes |
|---|---|---|
| $T_c$ - $T_r$ to $\lambda_p$ | $T_c$, $T_r$, $\lambda_p$ | How $\lambda_p$ affects the difference $T_c$ and $T_r$ and what kind of relationship exists between $T_c$ and $\lambda_p$ |
| $T_c$ - $T_r$ to $F$ | $T_c$, $T_r$, $F$ | How $F$ affects the difference between $T_c$ and $T_r$ and what kind of relationship exists between $T_c$ and $F$ |
| $T_c$ - $T_r$ to $Kn$, $\theta_a$, $\theta_z$ | $T_c$, $T_r$, $Kn$, $\theta_a$, $\theta_z$ | How solar parameters affect the difference between $T_c$ and $T_r$and what kind of relationship exists between $T_c$ and solar parameters |
| $T_c$ - $T_r$ to wind speed ($w$) | $T_c$, $T_r$,w | How wind speed affects the $T_c$ and $T_r$ and what kind of relationship exists between $T_c$ and wind speed |
| $T_c$ - $T_r$ to material variations | $T_c$, $T_r$, material properties in Table 2 | How different material properties affect the difference between $T_c$ and $T_r$ |

### 2.5. Evaluation of the relationship between $T_c$ and $T_r$

#### 2.5.1. Determination of the relationship between $T_c$ and $T_r$

The relative weight of variables and parameters is evaluated by the sensitivity analysis described in Section 2.4, which also indicates which kind of relationship, e.g. linear, exists between $T_c$ - $T_r$ and urban geometry parameters and climate variables. This can explain how urban geometry parameters and climate variables affect the difference between $T_c$ and $T_r$ and help to determine which kind of relationship between $T_c$ and geometric/climate variables can be constructed. In Section 2.4, the sensitivity analysis shows which parameters and variables are influential on $T_c$ and which kind of relationship exists between $T_c$ and these parameters.

In this section, the modelled $T_c$ and $T_r$ from TUF-3D were used to determine the relationship between $T_c$ and $T_r$. According to the sensitivity analysis in Section 2.4, we included the following variables, $\lambda_p$, $F$, Kn, $\theta_a$, $\theta_z$, in the relationship to estimate $T_c$ from $T_r$ in daytime (Eq. (5)) and included variables $\lambda_p$ and $F$ in the relationship to estimate $T_c$ from $T_r$ in nighttime (Eq. (6)). The relation between $F$ and $T_c$ is logarithmic according to the sensitivity analysis in Section 2.4. The relationships between other variables and $T_c$ are linear. About 6700 sets of $T_c$ and $T_r$ modelled by TUF-3D were used to regress the coefficients of Eq. (5) to estimate $T_c$ from $T_r$ in daytime. About 6500 sets of $T_c$ and $T_r$ modelled by TUF-3D under different structure and meteorological conditions in nighttime were used to regress the coefficients of Eq. (6) to estimate $T_c$ from $T_r$ for the nighttime case. In both cases, the relationships are generic, in the sense that they apply to all cases explored by the numerical experiments. The accuracy of such parameterization of $T_c$ is likely to increase when more predictive variables are applied. Since the sensitivity analysis suggests that a linear regression is sufficiently accurate, we determined the daytime parameterization of $T_c$ as a multilinear polynomial of the form:

$$T_c = a_1 * T_r + a_2 * \lambda_p + a_3 * \ln F + a_4 * \mathrm{Kn} + a_5 * \theta_a + a_6 * \theta_z + a_0 \quad (5)$$

and nighttime:

$$T_c = b_1 * T_r + b_2 * \lambda_p + b_3 * \ln(F) + b_0 \quad (6)$$

$a_0$~$a_6$ and $b_0$~$b_3$ are regressed coefficients based on the numerical experiments under the conditions of urban geometries and atmospheric forcing listed in Table 1 which can cover most conditions of urban geometric parameters and climate conditions. Thus, the Eqs. (5) and (6) apply to a broad range of urban and weather conditions.

#### 2.5.2. Validation of the relationship between $T_c$ and $T_r$

The high-spatial-resolution airborne thermal images with 0.5 m spatial resolution were used to extract the component temperatures such as temperatures of wall facets, rooftops, and roads. These images were observed at 12:40 pm on Aug 5, 2013 and 11:30 am on Oct 24, 2017. The building GIS data including building shape and height and Digital Surface Model (DSM) data were used to calculate the $\lambda_p$ and $F$ in order to estimate $T_c$ and $T_r$ from satellite data, while the high resolution airborne thermal camera data were applied to determine the component temperatures for each urban facet. For the high-resolution images, we obtained the mean component temperatures from different view images. The airborne thermal camera has a large FOV, so wall information can be acquired from the images. Then, $T_r$ was estimated by the nadir high-spatial-resolution airborne thermal images and used to estimate the $T_c$ based on the relationships constructed as described in this section (Eq. (5)). The $T_c$ estimated from component temperatures and $\lambda_p$ and $F$ (Eq. (3)) was used to validate the complete surface temperature estimated from $T_r$ and the relationships described in this section.

### 2.6. Estimation of $T_c$ from $T_r$

We have demonstrated how the relationship in Eqs. (5) and (6) can be applied to actual satellite images. Here we describe briefly the procedure applied, while the results are presented in Section 4.4.

Daytime thermal images acquired by Landsat TM in 2010 were used to retrieve daytime $T_r$ and ASTER nighttime thermal images acquired from Mar 13, 2013 and Aug 4, 2013 were used to retrieve $T_r$ at night. The $T_c$ images were then estimated by applying the relationships in Section 2.5 Eqs. (5) and (6).

The single channel method for $T_r$ retrieval was used in this study (Li et al., 2013). For Landsat TM data, the effective transmittance of the atmosphere in band 6 of Landsat 5, i.e. the upward and downward atmospheric thermal radiance can be estimated using the NASA Atmospheric Correction Parameter Calculator (http://atmcorr.gsfc.nasa.gov/) to obtain channel radiance observed at the top of the urban canopy. The band 13 radiance of ASTER AST 09T product is the ground-leaving in-band radiance including the emission of surface and the reflected radiance by the surface, and the sky thermal irradiance in band 13 of the ASTER AST 09T product was used to calculate the downwelling radiance for the UST retrieval (Sobrino et al., 2007). The radiance leaving urban canopy can be written as:

$$E(i) = \varepsilon(\mathrm{i})B(T_r(i)) + (1 - \varepsilon(\mathrm{i}))R_{at}^{\downarrow}(i) \quad (7)$$

In the Eq. (7), $\varepsilon(i)$ is the material emissvity of pixel $i$, calculated from the landcover and building GIS data as Yang et al. (2016) (see Section 3.3). B($T_r$(i)) is the upwelling radiance of pixel $i$ with radiometric temperature $T_r(i)$. $R_{at}^{\downarrow}(i)$ is the atmospheric downward radiance. When the effects of topography and geometric characteristics are considered, the thermal infrared ground-leaving radiance $E(i)$ comprises the emittance of facets in the observed built-up space, the reflected radiance by the facets within pixel $i$ and that by the neighboring scene elements.

The radiometric temperatures were first retrieved with Landsat TM and ASTER data, then the complete surface temperature was calculated using the retrieved radiometric temperature (Eqs. (5) and (6)). The urban geometric data and land use data were used to estimate the urban emissivity for the radiometric temperature. The building dataset and Digital Surface Model (DSM) were also used to calculate $\lambda_p$ and $F$. The seasonal effects on $T_c$ were analyzed using the Landsat TM and ASTER data.

## 3. Study area and data

### 3.1. Study area

Urban districts of Kowloon peninsula and Hong Kong Island across Hong Kong were selected as our study area (Fig. 1). In brief, Hong Kong is a coastal city in South China (22°17′N, 114°09′E), and this study area has been recognized as a compact city with high-density living (Chen et al., 2012). Specifically, urban districts of Kowloon peninsula and Hong Kong Island are highly urbanized with mixed land use and high population density (Peng et al., 2017). Historical development of these urbanized areas has also resulted in commercial areas with high-density high-rise built environment for decades (Peng et al., 2017). Nowadays, there are even two high-rise buildings with > 400 m across the study area (the International Finance Centre and International Commerce Centre). Due to this high-rise, high-density urban environment, urban canyons have formed to influence microclimate significantly (Chen et al., 2012). In this condition, the remote sensing observation is also limited to part of urban facets. The observed radiometric surface temperature cannot represent the real urban surface temperature in such compacted city. Thus, the estimation of $T_c$ is crucially important for urban climate research in Hong Kong, as a high quality thermal dataset should enhance the estimation of microclimate across a compact environment in a three-dimensional context.

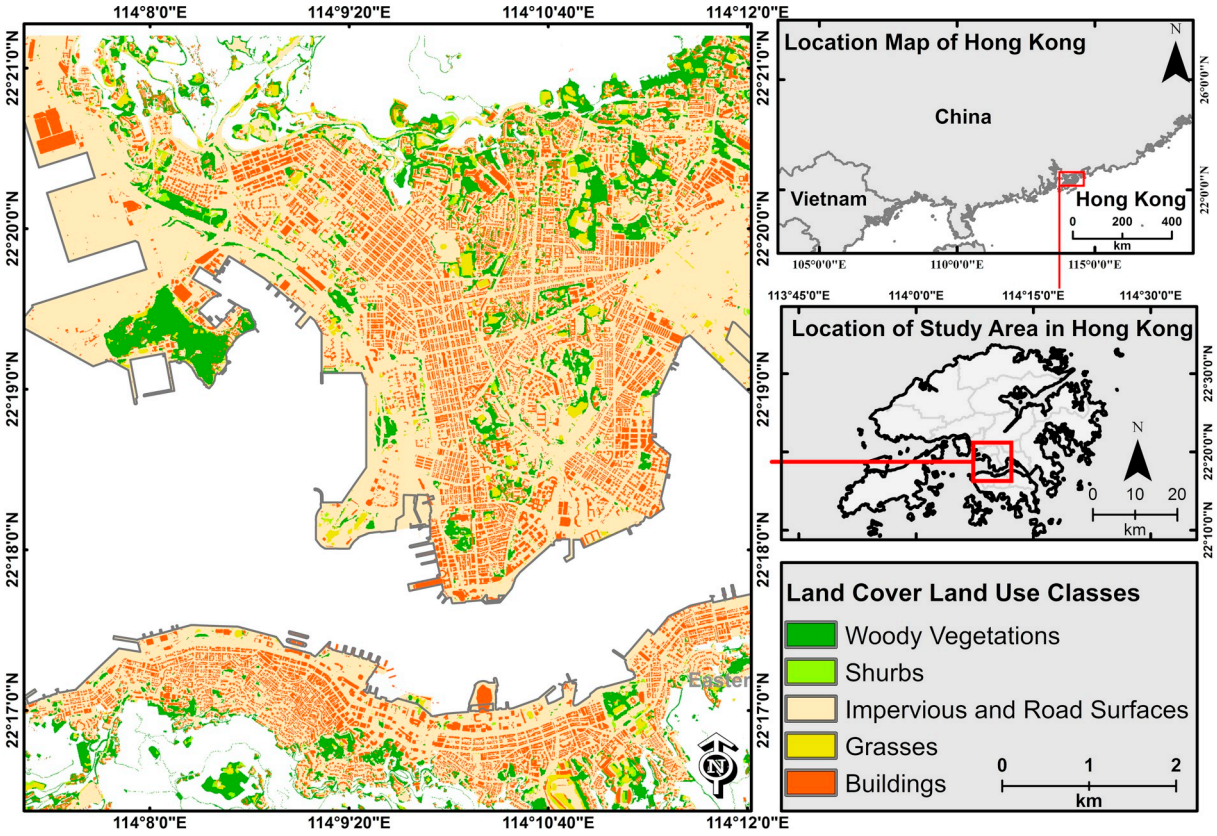



**Fig. 1.** Study area: land uses in Kowloon peninsula and the Hong Kong Island.

### 3.2. Thermal remote sensing data

Landsat TM and ASTER data were used to estimate $T_c$ in Hong Kong. The high spatial resolution thermal image data (Fig. 2) captured on Aug 5, 2013 and Oct 24, 2017 were used in this study for validation. These images are observed at the nadir of the central image line but the FOV of airborne thermal camera is large, so the images overlap, i.e. in different images there is the LST of the same target at different view angles. The estimated complete surface temperature was validated using the component temperatures (wall facets, rooftop and road) captured by the high resolution airborne thermal images and building data (Fig. 2a to d). Additionally, the building data and Digital Surface Model (DSM) data at 1 m spatial resolution were used to calculate $\lambda_p$ and $F$ to estimate the complete surface temperature. More information about building data and LiDAR data can be found in Yang et al. (2016). The data acquired by satellite and airborne platforms used in this study are listed in Table 4.

### 3.3. Land use and building information

We used airborne LiDAR data with 1 m spatial resolution and the building GIS data provided by the Hong Kong Civil Engineering and Development Department and Hong Kong Lands Department (Lai et al., 2012) (Fig. 1). The LiDAR data were collected in December 2010 and January 2011 and used to determine and map the building heights (Fig. 3). Land use data provided by the Hong Kong Planning Department and the 2010 building GIS data were used to estimate and map the material emissivity of Hong Kong (Fig. 1). The overall classification accuracy of the land – use data in urban areas was 96% (according to the Hong Kong Planning Department). The land use classification data provide land cover information, e.g. tree, grassland and impervious surface with a spatial resolution of 6 m. Building GIS data were used to distinguish the impervious surface in buildings and road pavements (Fig. 1). More information about emissivity estimation can be referred to Yang et al. (2016).

The building GIS data and building heights (Fig. 3) were used to calculate $\lambda_p$ and $F$. The $\lambda_p$ with building data was calculated as the ratio of the building roof area to the area of a pixel, i.e. 30 m × 30 m for Landsat or 90 m × 90 m for ASTER. $F$ was calculated as the ratio of the building wall area to the area of a pixel.

### 3.4. Ground-level meteorological data

The meteorological data used in this study (Table 5) were collected at the weather station located at the headquarters of the Hong Kong Observatory. Observations used in the experiments were limited to the time period between 0 am and 24 pm local time of sunny days in each month of year 2010. These days were selected because of the cloudless conditions. The air temperature ranges from 5.2 to 32.7 °C. Wind speed ranges from 0.1 to 4.3 m $s^{-1}$ since in Hong Kong there are many high-rise buildings which reduce wind speed in the surface layer. The highest solar irradiance is 1013.89 W/$m^2$ at noon on July 1st 2010. These meteorological data can cover most subtropical and mid-latitude climate conditions. Extreme cold areas may need further study.

## 4. Results

The results of the sensitivity analysis described in Section 2.3 are presented first (Section 4.1), followed (Section 4.2) by the determination of the simple model described in Section 2.4. The model is then evaluated against the high resolution TIR image data (Section 4.3) and applied to actual Landsat TM and ASTER image data (Section 4.4).

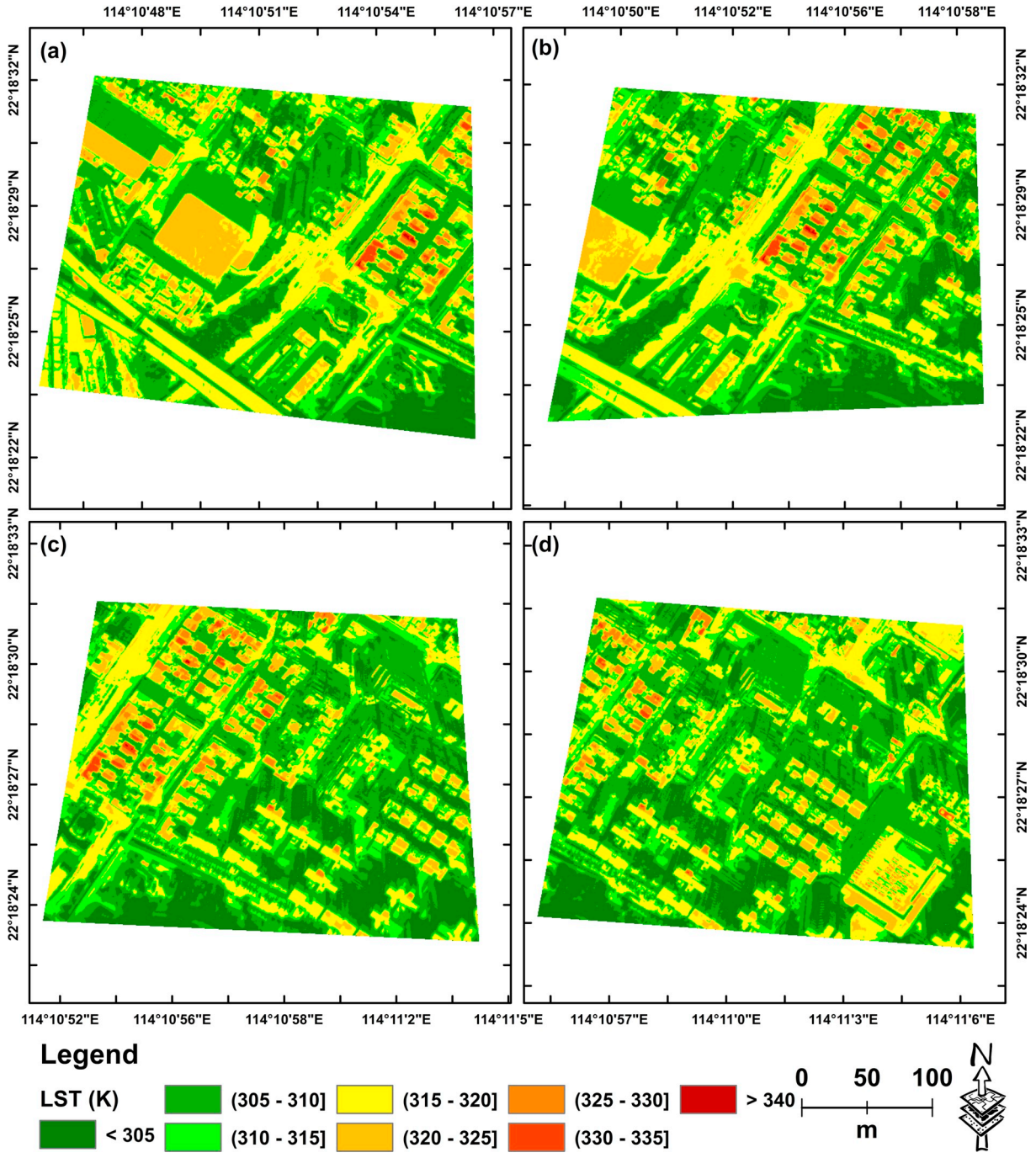



**Fig. 2.** High spatial resolution thermal images acquired on Aug 5, 2013.

**Table 4**
Overview of satellite and airborne Thermal InfraRed (TIR) images used in this study.

| Data | Date | Local time | Resolution (m) | Purpose |
|---|---|---|---|---|
| Landsat TM Band 6 | Jan 14, 2010 | 10:37 am | 30 (resampled) | Retrieve $T_r$ and $T_c$ |
| | Mar 26, 2010 | 10:43 am | | |
| | Sept 18, 2010 | 10:42 am | | |
| | Oct 29, 2010 | 10:36 am | | |
| | Nov 11, 2010 | 10:36 am | | |
| | Dec 23, 2010 | 10:42 am | | |
| ASTER band 13 | Mar 13, 2013 | 10:36 pm | 90 | |
| | Aug 4, 2013 | 10:36 pm | | |
| Thermal images from thermal camera (FLIR T650sc) on airborne helicopter (500 m) | Aug 5, 2013 | 12:40 pm | 0.5 | Validation |
| | Oct 24, 2017 | 11:30 am | | |

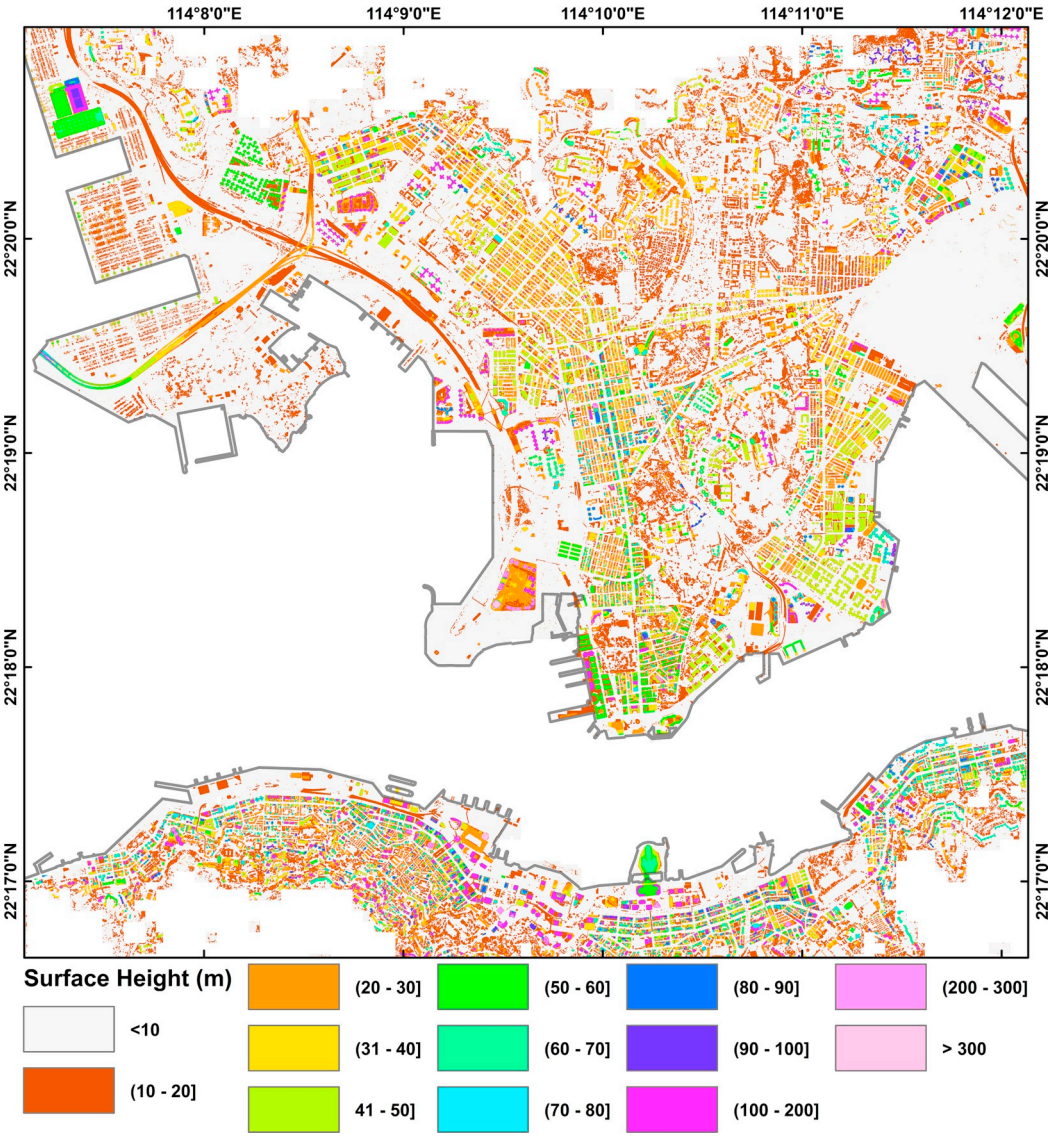



**Fig. 3.** Building heights of Kowloon peninsula and the Hong Kong Island.

**Table 5**
Overview of the meteorological data used in this study.

| Variable | Description (units) | Date | Duration (hourly) |
|---|---|---|---|
| Solar irradiance | $W/m^2$ | Feb 27, 2010; Mar 10, 2010; Apr 11, 2010; May 25, 2010; Jul 1, 2010; Aug 2, 2010; Sept 17, 2010; Oct 28, 2010; Nov 27, 2010; Dec 7, 2010 | 0–24 |
| Wind speed | $m\ s^{-1}$ | | |
| Air temperature | °C | | |
| Air pressure at ground surface | mb | | |

### 4.1. Sensitivity analysis of the relationship between $T_c$ and $T_r$

#### 4.1.1. Effects of $\lambda_p$ on difference between $T_c$ and $T_r$

A linear relationship between the difference ($T_c$ - $T_r$) and $\lambda_p$ was found for different solar and H/L daytime conditions (Fig. 4). In Fig. 4, the radiative and thermal properties are set as Group 3 in Table 2. This experiment was performed at constant values of H/L, wind speed, solar azimuth and zenith angles, i.e. changes in ($T_c$ - $T_r$) were due to changes in $\lambda_p$ only. Overall, $T_c$ - $T_r$ increased in magnitude (absolute difference) with $\lambda_p$. With the increase of $\lambda_p$, the fraction of irradiance on street/road facets decreases, while the fraction of irradiance on rooftop facets increases (Yang and Li, 2015). At the same time, the sensible heat flux at wall and street facets decreases with $\lambda_p$, while the sensible heat flux at roof facets remains nearly constant (Appendix Fig. 1a). The overall sensible heat flux decreases with $\lambda_p$ due to the skimming effect (Grimmond and Oke, 1999). During daytime, irradiance on street and wall facets decreases with increasing $\lambda_p$ because of the reduced sky view factor. Additionally, the proximity between street and wall surfaces reduces sky view factors and increases drag on the airflow reducing the convective heat transfer from the urban canopy to the surface layer (Nazarian and Kleissl, 2015). The reduced irradiance leads to lower wall surface temperature and sensible heat flux at wall facets. Note that the dominant factor influencing canopy surface temperature during daytime is solar radiation. This makes the wall and street surface temperature to decrease with increasing $\lambda_p$. Moreover, the shading effect makes surface temperature of street and wall facets lower than roof facets. With the increase of $\lambda_p$, a greater portion of the 3D facets cannot be observed by a nadir viewing imaging radiometer. At the same time, $T_c$ decreases with increasing $\lambda_p$ due to the decrease of wall and street surface temperatures (Appendix Fig. 2). The change of $T_r$ with $\lambda_p$ is not consistent and depends on the solar zenith angle and building H/L (Appendix Fig. 2) since both the solar angle and building H/L ratio

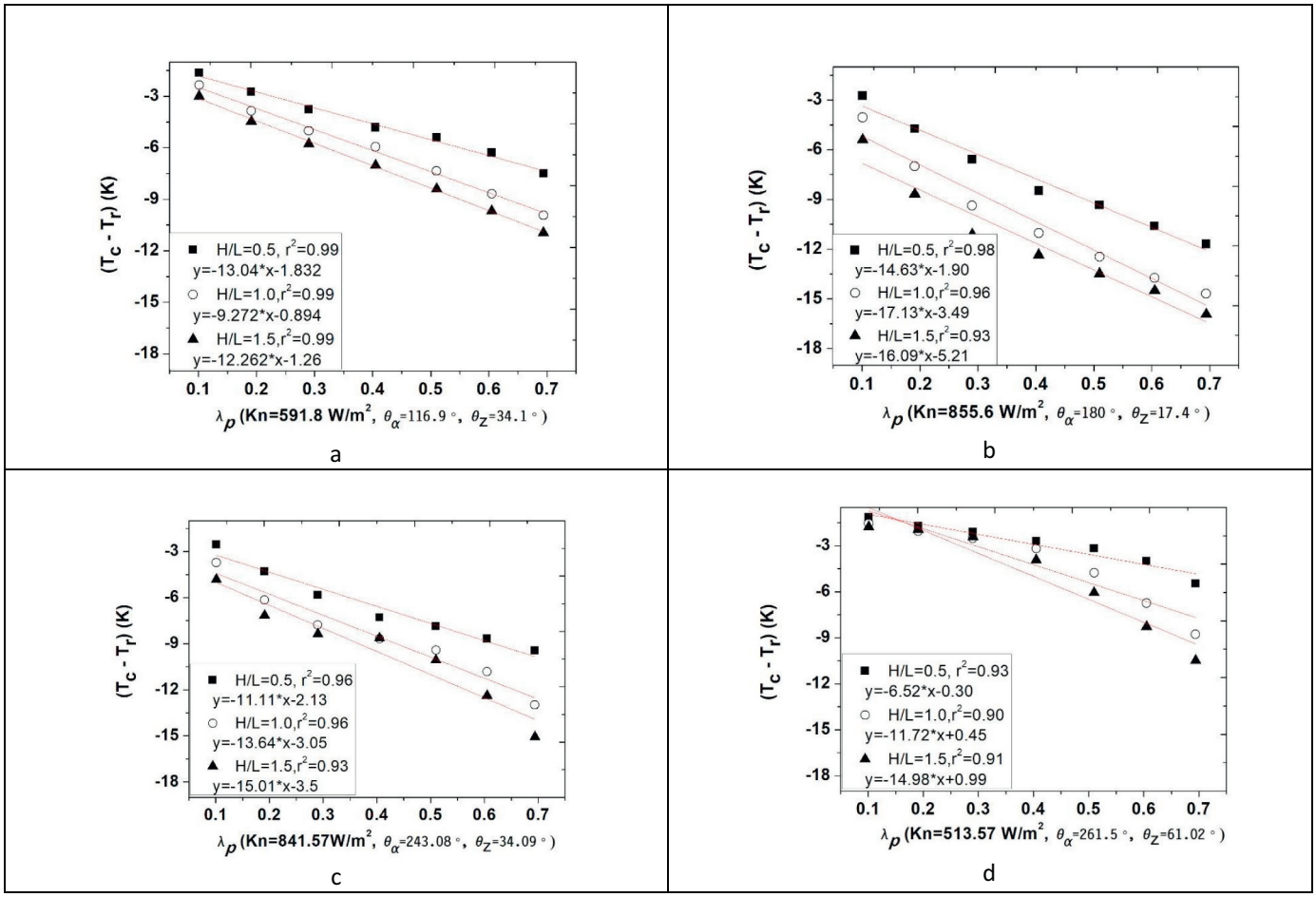



**Fig. 4.** Relationships between the difference ($T_c$ - $T_r$) and $\lambda_p$ under four different daytime solar conditions.

determine shadows. The difference between $T_c$ and $T_r$ changes with local solar time because of the solar position and irradiance. At lower solar zenith angles (Fig. 4b), the difference between $T_c$ and $T_r$ is larger than at higher solar zenith angles (Fig. 4d). The linear dependence of ($T_c$ - $T_r$) on $\lambda_p$ holds in all cases, but the slope changes with H/L and solar position, which should be taken into account in a generalized model. Street orientation also affects the irradiance and the shadow distribution and then affects both radiative and convective heat transfer. The material properties of roof, street and wall also affect the surface temperature distribution. This study did not consider the street orientation and material properties, which should be investigated in future work.

In these experiments, the decrease in wall facet temperature at night was generally smaller than for rooftop temperature. One reason is the attenuation of radiation loss because of radiative trapping in the urban canyons compared to rapid radiative cooling of rooftops (Martilli et al., 2002). Overall, the sensible heat fluxes at roof facets and wall facets are much smaller than in daytime. The sensible heat flux at roof facets is close to zero and much smaller than the sensible heat flux at wall and street facets (Appendix Fig. 1). This is because the rooftop surface temperature is much lower than the wall surface temperature at night (Nazarian and Kleissl, 2015). This thus induces a different urban surface temperature distribution compared with daytime, and this difference is also captured by the relationship between ($T_c$ - $T_r$) and $\lambda_p$ at night (Fig. 5). In addition, radiative trapping increases with $\lambda_p$, thus ($T_c$ - $T_r$) at night increases with increasing $\lambda_p$. With increasing $\lambda_p$, a larger rooftop fractional area is captured by a nadir viewing imaging radiometer. The high-density of buildings can reduce the effectiveness of walls in radiative and convective dissipation of excess energy, which results in higher wall temperature than rooftops at night (Coutts et al., 2007). These make ($T_c$ - $T_r$) at night increase with increasing $\lambda_p$. Higher $\lambda_p$ implies a smaller sky view factor and results in higher surface temperature within urban canyons. The cooling rate of wall and ground facets is much smaller than that of roof facets, thus the temperature of the wall surface is higher than rooftop, even in the early morning before sunrise (Kusaka and Kimura, 2004; Nazarian and Kleissl, 2015). This results in nighttime $T_r$ being lower than $T_c$. The material properties also affect the cooling rate of urban surfaces, as described in a later section.

#### 4.1.2. *Effects of F on the difference between $T_c$ and $T_r$*

When $\lambda_p$ is constant, $F$ and aspect ratio increase with H/L. During daytime, the relationship between ($T_c$ - $T_r$) and $F$ is logarithmic when aspect ratio is smaller than 3.5 (Fig. 6). When the aspect ratio and $F$ increase, the street canyon becomes narrower and less solar radiation penetrates into the street canyon, thus irradiance onto street and wall facets decreases (Ali-Toudert and Mayer, 2006; Lemonsu et al., 2004; Nazarian and Kleissl, 2015; Yang and Li, 2015). The increase of aspect ratio contributes to the decrease of sensible heat flux at wall and ground facets (Nazarian and Kleissl, 2015). The total sensible heat flux increases with increasing aspect ratio, since the frontal area index and displacement height increase and, therefore, the aerodynamic resistance decreases. In daytime the energy loss by sensible heat exchange is mainly from rooftops (Martilli et al., 2002), while the irradiance onto rooftop facets does not vary since the $\lambda_p$ does not change. Overall, these changes lead to a lower rooftop surface temperature. The difference between $T_c$ and $T_r$ increases gently with increasing $F$ (Fig. 6). The decrease in irradiance is the dominant driver of wall and ground surface temperature, which still decreases notwithstanding the decrease in

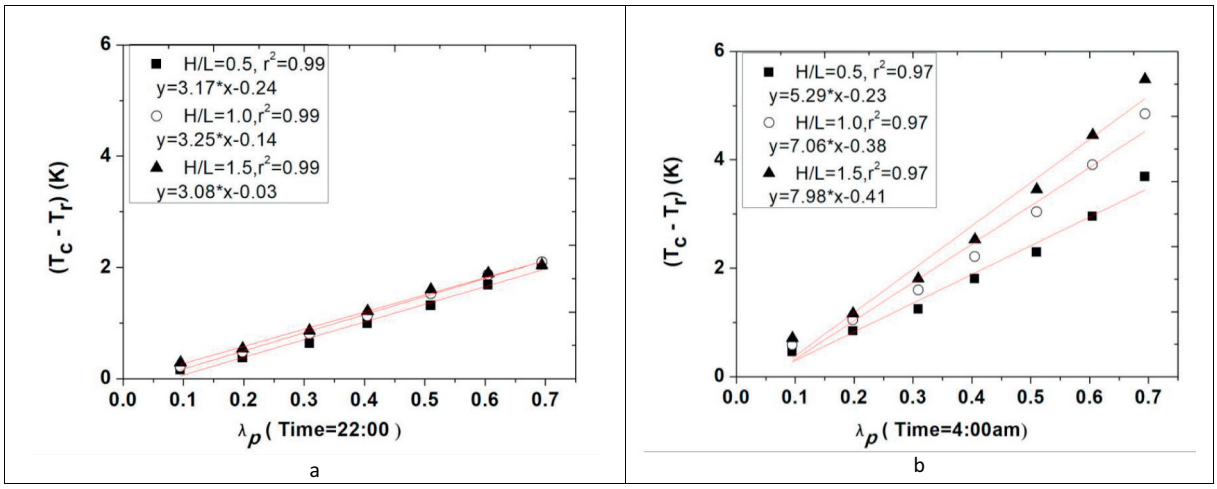



**Fig. 5.** Relationship between the nighttime difference ($T_c$ - $T_r$) and $\lambda_p$.

sensible heat flux with *F*. When the solar zenith angle $\theta_z$ is larger than 0, the wall and ground surface temperatures decrease less than when $\theta_z$ is equal to 0 (Fig. 6d) and $T_c - T_r$ levels off when F is higher than a threshold F*, which depends on irradiance and $\theta_z$ (Fig. 6).

At night, $T_c - T_r$ increases with *F* at constant $\lambda_p$ and then saturates (Fig. 7). A higher aspect ratio reduces the sky view factor, longwave emittance and convective heat transfer to the atmospheric boundary layer. The sensible heat flux at wall and ground facets decreases with increasing aspect ratio (Nazarian and Kleissl, 2015). The cooling rate of wall and ground facet surfaces at night decreases with increasing aspect ratio, everything else being the same (Nazarian and Kleissl, 2015). Road and wall facets are then cooling less than rooftop facets and also contributing to a road and wall facet temperature higher than rooftop facet temperature, resulting in an increase in $T_c - T_r$ with the aspect ratio. Convective heat exchange between wall facets and the atmospheric boundary layer increases with *F*, due to the effect of *F* on the temperature difference between the urban canyon and atmospheric boundary layer. This makes the wall surface temperature decrease, everything else being the same, and $T_c - T_r$ to level off past an initial increase with *F* (Fig. 7). The difference between $T_c$ and $T_r$ increases with

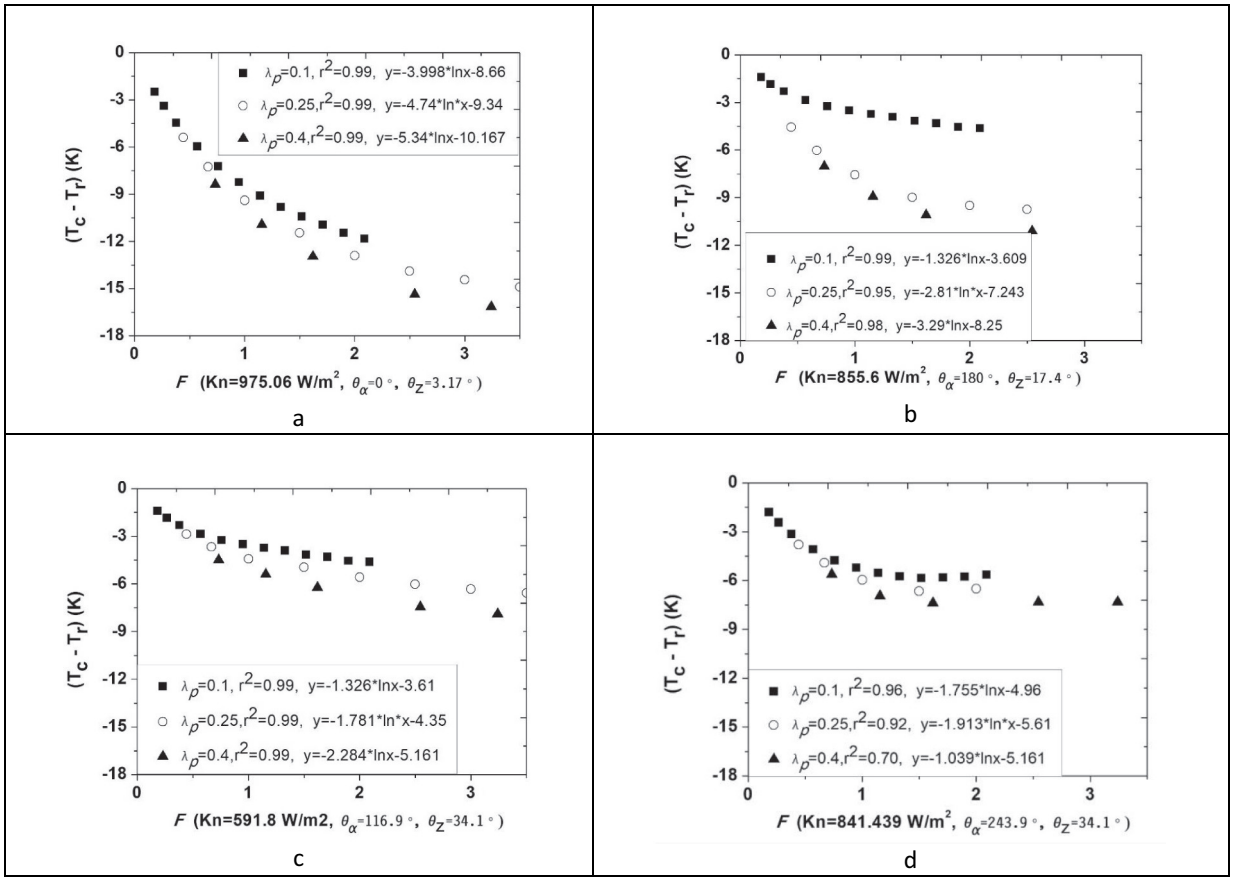



**Fig. 6.** Relationship between the daytime difference ($T_c$ - $T_r$) and *F* under different solar conditions.

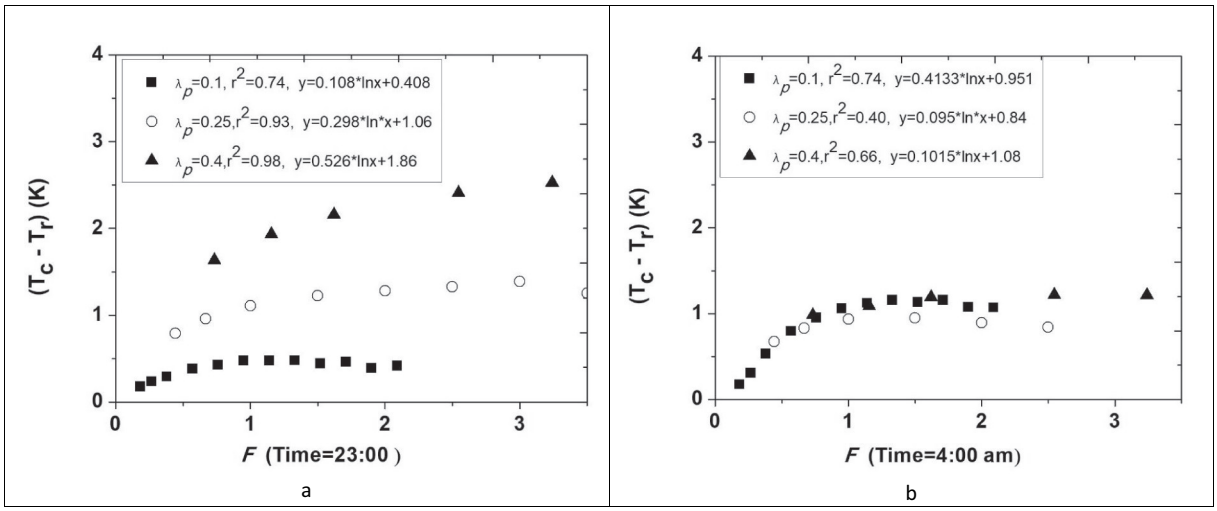



**Fig. 7.** Relationship between the nighttime difference ($T_c$ - $T_r$) and $F$.

the 3D complexity of the observed urban target. It approaches zero with both $F$ and $\lambda_p$ approaching zero (i.e. for a flat target) and it is largest with $F = 4$ and $\lambda_p = 0.4$ in Figs. 6 and 7. A higher F-value at constant $\lambda_p$ applies to taller buildings at constant areal (roof) density, while a higher $\lambda_p$ at constant F applies to denser but lower buildings. In both cases an increase in either F or $\lambda_p$ implies that more building facets cannot be observed by a nadir looking radiometer, thus explaining the increasing difference between $T_c$ and $T_r$.

#### 4.1.3. Effects of solar radiation on the difference between $T_c$ and $T_r$

The irradiance onto urban surfaces changes with the solar angle, shading pattern and shortwave radiation intensity (Nazarian et al., 2017). The surface temperatures of road, rooftop and wall facets undergo a very different diurnal thermal cycle due to the solar position, urban geometry and material properties (Nazarian and Kleissl, 2015). This process contributes to the spatial variability of urban surface temperature and of turbulent heat transfer (Nazarian et al., 2018a, 2018b). Uneven irradiance caused by urban geometry and materials is the main driver of the spatial variability of daytime surface temperature under cloudless conditions, which results in the difference between $T_c$ and $T_r$. The surface temperature of roads and wall facets is lower than roof temperature, due to the shadowing effect. The solar zenith angle and azimuth angle vary by the hour and day of year, which cast shadows at different locations within the urban canopy, thus determining the spatial variability of UST. Additionally, the magnitude of surface temperature heterogeneity changes with solar irradiance, e.g. surface temperature heterogeneity is higher in summer than in winter in Hong Kong. Fig. 8 showed the effects of solar irradiance and solar position on ($T_c$ - $T_r$) when $\lambda_p = 0.25$ and H/L = 0.5. This study used actual observations of solar irradiance on three days (Fig. 8b). The results showed that when the irradiance is smaller, e.g. case 3 in Fig. 8b, ($T_c$ - $T_r$) is smaller. When the irradiance increases, ($T_c$ - $T_r$) increases, since the rooftop temperature increases more than the wall temperature (Fig. 10b, case 1 and case 2). The higher irradiance heats up the rooftop facets, which makes the $T_r$ observed by remote sensors higher than $T_c$. The daytime solar radiation has little impact on the nighttime $T_c - T_r$ 3 h after sunset, e.g. 9:00 pm (Fig. 8a).

#### 4.1.4. Effects of wind speed on the difference between $T_c$ and $T_r$

TUF-3D is not originally designed for detailed assessments of the impacts of wind speed on surface temperature. This study adopted, however, a first-order evaluation of wind speed effects on $T_c - T_r$, assuming $T_r$ to be observed at nadir. In our numerical experiments (see Section 2.2), wind speed at twice the building height was varied within the range 1 to 6 m $s^{-1}$. The results show that $T_c - T_r$ decreases with increasing wind speed (Fig. 9). This effect is particularly strong during daytime for a neighborhood with a large wall area, in which case directional shortwave irradiance generates a larger surface temperature heterogeneity which is modulated by wind speed. On average, our experiments give a sensitivity of $T_c - T_r$ to wind speed, with a 0.83 K

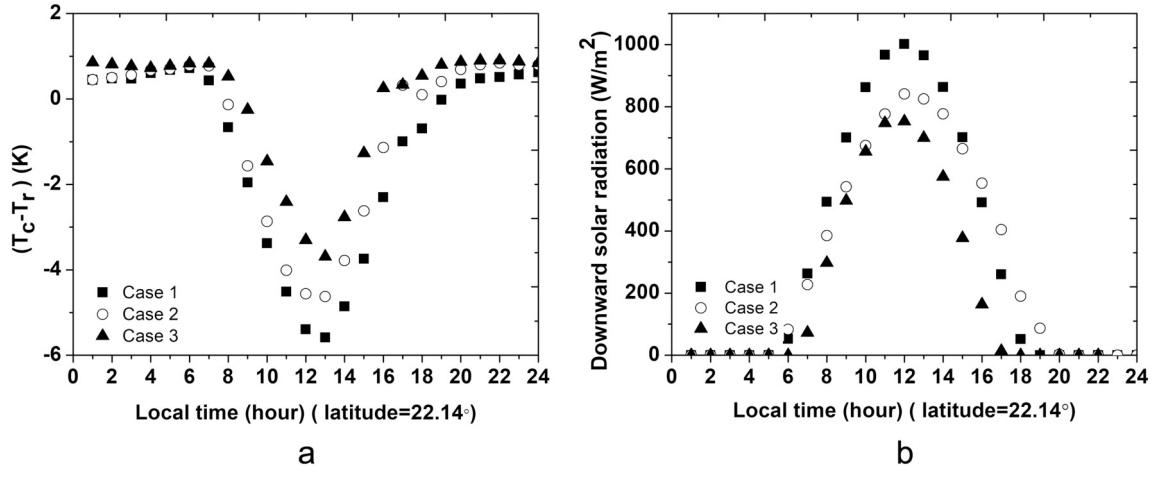



**Fig. 8.** Sensitivity of $T_c - T_r$ to irradiance: a) $T_c - T_r$ for cases 1 to 3 and; b) irradiance cases 1 to 3 as applied in a).

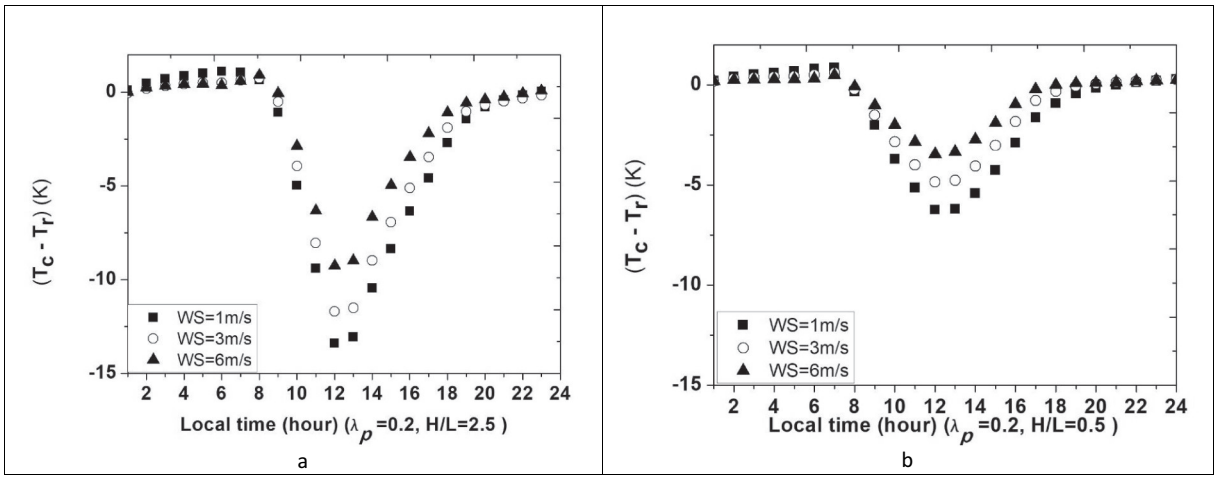



**Fig. 9.** Sensitivity of $T_c - T_r$ to wind speed under different conditions: a, $\lambda_p = 0.2$, H/L = 2.5; b, $\lambda_p = 0.2$, H/L = 0.5.

reduction of $T_c - T_r$ per 1 m $s^{-1}$ increase in wind speed when $\lambda_p = 0.2$ and H/L = 2.5. These reductions of $T_c - T_r$ with wind speed vary with solar radiation and building density and height (Fig. 9).

#### 4.1.5. Sensitivity of $T_c - T_r$ to material properties

The material heterogeneity also causes thermal heterogeneity, but it is difficult to obtain exact information on materials in a city. Based on the material properties provided by Stewart et al. (2014), the effects of material properties on $T_c - T_r$ were studied. Under different geometric and meteorological daytime conditions, the different materials can cause a 1.5 °C difference in $T_c - T_r$ (Fig. 10). The differences in $T_c - T_r$ depend on the material distribution and solar position, although differences caused by material properties remain much lower than $T_c - T_r$. We still recommend however, that the local material properties should be used in numerical experiments to study the dependence of $T_c - T_r$ on urban conditions. The impact of material properties on $T_c - T_r$ is smaller during nighttime, i.e. < 0.5 K and increasing with $\lambda_p$ (Fig. 11).

### 4.2. Development of a simple empirical model to estimate $T_c$-$T_r$

The dependence of $T_c$-$T_r$ on geometric and climate variables and parameters has been explored in Section 4.1. This analysis suggests that $T_c$-$T_r$ depends linearly on $\lambda_p$ and the solar parameters (Kn, $\theta_a$, $\theta_z$), while the dependence on $F$ is logarithmic.

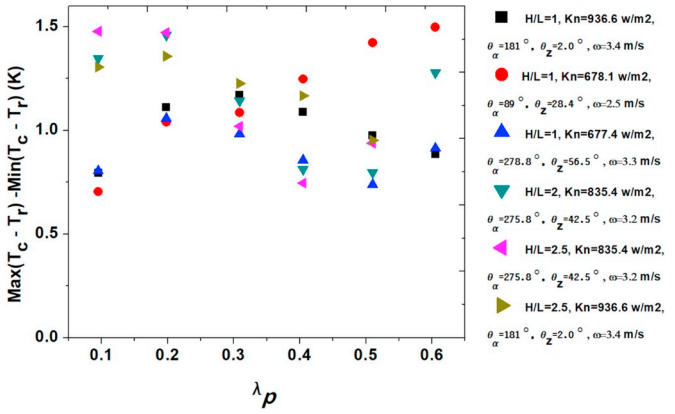



**Fig. 10.** Impact of material properties on daytime $T_c$-$T_r$: (max($T_c$-$T_r$) - min($T_c$-$T_r$)) obtained with the TUF – 3D numerical experiments and applying different combinations of material properties in Table 2. (The parameter values applying to each experiment are listed in the legend: H/L = ratio of building height to length; Kn = solar irradiance; $\theta_a$ = sun azimuth angle; $\theta_z$ = sun zenith angle; $\omega$ = wind speed).

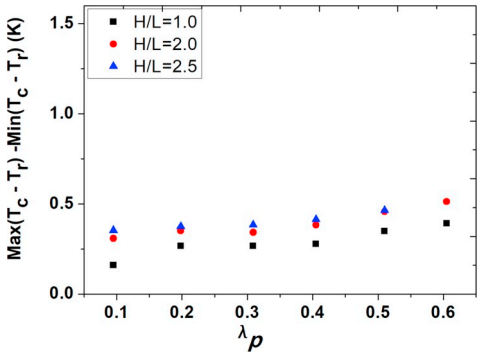



**Fig. 11.** Impact of material properties on nighttime $T_c - T_r$: (max($T_c$-$T_r$) - min($T_c$-$T_r$)) obtained with the TUF – 3D numerical experiments and applying different combinations of material properties in Table 2. (The parameter values applying to each experiment are listed in the legend: H/L = ratio of building height to length).

Building upon these findings, a simple empirical model (see Eq. (5)) to estimate $T_c$ from $T_r$. $f_d$ was constructed for daytime conditions by fitting Eq. (5) to the pseudo – observations generated by numerical experiments (Table 6). Two options were explored: a) by binning the pseudo – observations according to wind speed in steps of 1 $ms^{-1}$ (see first four cases in Table 6); b) by pooling the pseudo – observations for the entire range in wind – speed (Eq. (8)). The RMSE increases with the wind speed (Table 6), but the RMSE for case (b) is still acceptable and not much larger than in three out of four (a) – cases, with $r^2 = 0.97$ for case (b). We can then conclude that a simple empirical model applies to a broad range of geometry and climate conditions and that it is not strictly needed to include wind–speed as a predictive variable. This is the empirical model we evaluated against high resolution airborne TIR images (Section 4.3) and applied to satellite TIR (Section 4.4).

Larger RMSEs were found when fitting the same model to pseudo – observations applying to sunrise (8 am) and sunset (5 pm), due to heat convection rather than solar irradiance being the main driver of UST at this time of the day (moreover with $T_c$-$T_r$ being rather small). In contrast, the spatial variability in UST around noon, i.e. from 11 am to 3 pm is driven by uneven irradiance associated with urban geometry. Accordingly, a smaller bias for estimated $T_c$, i.e. RMSE < 1 K, was achieved by combining meteorological and urban geometry parameters. The numerical experiments suggest that the inclusion of urban geometry parameters is most significant in modelling $T_c$ in the afternoon.

When the wind speed ranges from 0 to 6 m $s^{-1}$, the relationship to estimate $T_c$ from $T_r$ at daytime can be written as:

**Table 6**
Estimation of daytime $T_c$ from $T_r$: regression relationships for different ranges in wind speed.

| Wind speed (m $s^{-1}$) | Regression model | $r^2$ | RMSE (K) |
|---|---|---|---|
| 0–1 | $Tc = 1.065 * T_r - 2.883 * \lambda_p - 0.093 * \ln(F) - 0.021 * Kn + 0.014 * \theta_a - 0.088 * \theta_z - 10.509$ | 0.94 | 0.70 |
| 1–2 | $Tc = 0.930 * T_r - 6.757 * \lambda_p - 0.856 * \ln(F) - 0.006 * Kn - 0.003 * \theta_a + 0.053 * \theta_z + 20.003$ | 0.97 | 1.15 |
| 2–3 | $Tc = 0.927 * T_r - 6.509 * \lambda_p - 1.023 * \ln(F) + 0.003 * Kn - 0.020 * \theta_a + 0.181 * \theta_z + 14.384$ | 0.97 | 1.31 |
| 3–4 | $Tc = 0.773 * T_r - 3.712 * \lambda_p - 1.730 * \ln(F) + 0.004 * Kn - 0.001 * \theta_a + 0.139 * \theta_z + 59.377$ | 0.96 | 1.58 |

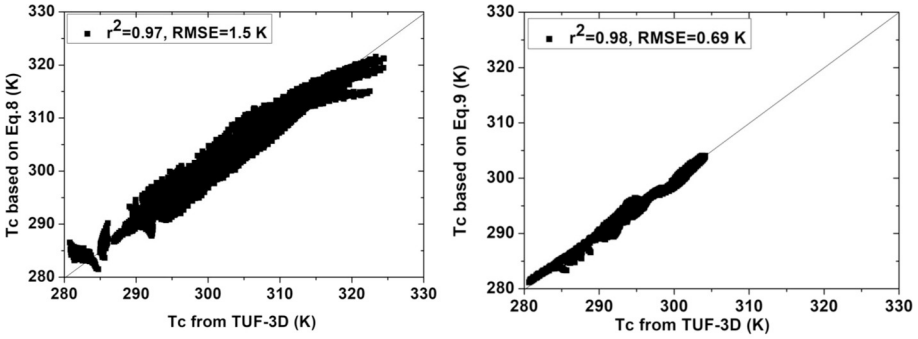



**Fig. 12.** Scatter plot between actual and estimated $T_c$ in the process of determining the coefficients: a, $T_c$ from Eq. (8); b, $T_c$ from Eq. (9).

$$T_c = 0.913 * T_r - 5.390 * \lambda_p - 1.090 * \ln(F) + 0.001 * Kn - 0.013 * \theta_a + 0.139 * \theta_z + 20.598 \quad (8)$$

Which gives $r^2 = 0.97$, RMSE = 1.500 K. The plot of $T_c$ simulated by TUF-3D and estimated by Eq. (8) is presented in Fig. 12a.

During nighttime, $T_c$-$T_r$ levels off and it is rather small from 9 pm to 6 am (Fig. 8), while wind speed has a limited effect (Fig. 9). Urban geometry still affects the energy exchange and yields uneven cooling during nighttime, thus leading to the predictive parameters to include in our simple empirical model (see Eq. (6)). Finally, the relationship to estimate $T_c$ from $T_r$ at nighttime can be written as:

$$T_c = 0.927 * T_r + 3.455 * \lambda_p + 0.184 * \ln(F) + 21.320 \quad (9)$$

Which gives $r^2 = 0.98$, RMSE = 0.690 K. The plot of $T_c$ simulated by TUF-3D and estimated by Eq. (9) is presented in Fig. 12b.

When $F$ is close to 0 and the surface is flat, $T_c$ tends to $T_r$. The developed logarithmic function (see Eqs. (8) and (9)) would give undefined values in the limiting case $F = 0$. Even very small values of $F$, e.g. $F = 0.001$ and $\lambda_p = 0.1$, however, give a realistic value of 0.045 K for $T_c$-$T_r$ when applying Eq. (9) to a nearly flat surface with 280 K. To avoid any ambiguity, therefore, a threshold should be defined, e.g. $F > 0.001$, to constrain the range of validity of Eqs. (8) and (9).

This empirical model was applied to estimate $T_c$ from $T_r$ retrieved from the ASTER nighttime data (see Section 4.4).

### 4.3. Evaluation with high resolution airborne thermal data

Two experiments were conducted to evaluate our simple empirical model using high spatial resolution thermal infrared image data acquired on Oct 24, 2017 and Aug 5, 2013, where Oct 24, 2017 represents a day with lower solar irradiance (700 W/$m^2$) and Aug 5, 2013 was a day with higher irradiance (878.2 W/$m^2$). In addition, wind speed was rather low and similar, i.e. 2–3 m $s^{-1}$ on both dates, so that we expected a larger thermal heterogeneity.

According to the methodology described above, we calculated the component temperatures within each 30 m × 30 m grid by averaging the 0.5 m × 0.5 m surface temperature for each surface type. Then we obtained the $T_c$ from these component temperatures by Eq. (3). Then we estimated $T_c$ from $T_r$ by applying our Eq. (8) and evaluated our estimates against the Tc values obtained from the high resolution thermal images. We then compared these two sets of $T_c$ (Fig. 13a and b). We used the urban geometric parameters in our empirical relationships and the component temperatures derived from high-resolution images (Fig. 2) at different view angles to determine the wall facet temperatures and the reference $T_c$. This validation gave reasonably accurate estimates of $T_c$, consistent with the expected accuracy of our empirical model (Eq. (8)), with $r^2 = 0.75$ and RMSE = 1.09 K on Aug 5, 2013 and $r^2 = 0.86$ and RMSE = 1.86 K on Oct 24, 2017 (Fig. 13b).

### 4.4. Complete urban surface temperature from satellite data

Finally, we estimated the daytime and nighttime complete urban surface temperature by applying our empirical models to Landsat TM and ASTER TIR image data respectively (Figs. 14 and 15).

The previous sections and findings suggested that the procedure (Eq. (8)) can be applied to an entire Landsat TM Band 6 image. The results showed that $T_c$ over built-up areas was lower than over impervious areas and that during daytime, $T_r$ was generally higher than $T_c$. The mean value of ($T_c$-$T_r$) was −2.15 K while in extreme cases it reached −6 K in built-up areas on Dec 23, 2010. $T_c$-$T_r$ has a strong seasonal trend associated with urban morphology and solar position (Table 7). For example, the mean value of $T_c$-$T_r$ on Sept 18, 2018, 2010 was −4.98 K with extreme values as low as −10 K across built-up areas. This was possibly due to solar irradiance being the main driver of spatial variability of UST in daytime during the summer, when $T_r$ is much higher than $T_c$, also taking into account the impact of shadows in the urban canyon, as determined by solar position. On the other hand, the solar elevation on Sept 18, 2010 was much higher than on the other days (14 Jan 2010; 26 Mar 2010; Oct 29, 2010; Nov 11, 2010; Dec 23, 2010), which determined the extreme ($T_c$-$T_r$) values. The higher solar elevation leads to rooftop temperatures higher than wall facet temperatures, since solar irradiance on the wall facets is lower. This result is also demonstrated by an increase in ($T_c$-$T_r$) when the solar elevation decreases and solar irradiance on the wall facets increases.

$T_c$ was higher than $T_r$ in several built-up areas during spring, autumn and winter, while $T_c$ was lower than $T_r$ in almost all urban areas during summer. The mean absolute value of ($T_c$ – $T_r$) was nearly equal to the absolute value of mean ($T_c$ – $T_r$) on Sept 8, 2010, while the absolute value of mean ($T_c$ – $T_r$) on the other dates was much lower than the mean absolute value (Table 7). This is possibly due to a lower $T_r$

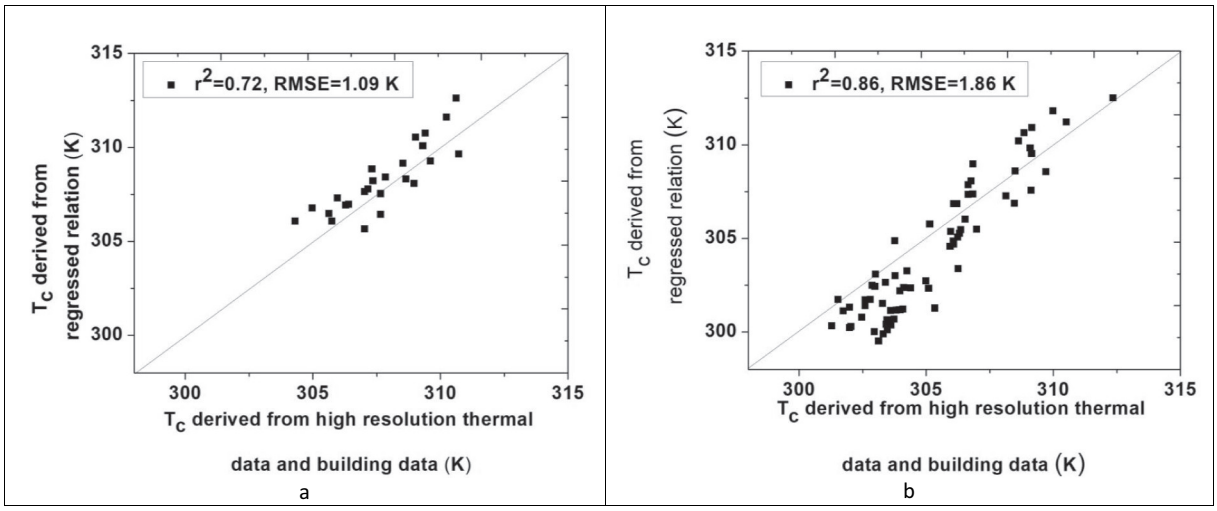



**Fig. 13.** Comparison between $T_c$ derived from $T_r$ and $T_c$ retrieved from component temperatures based on high resolution airborne thermal images: a, on Aug 5, 2013; b, Oct 24, 2017.

across several built-up areas in non-summer seasons because of lower solar elevation angle, especially in the areas with fewer high-rise buildings and lower density.

The nighttime $T_c$ was estimated by applying Eq. (9) with ASTER-TIR radiometric data and building data. The $T_c$ was found to be higher than $T_r$ over built-up areas, with the difference reaching 2 K (Fig. 14). The Nighttime ($T_c$ - $T_r$) was higher in spring than in summer, while the daytime ($T_c$ - $T_r$) was lower in summer than in winter. Average and standard deviation of ($T_c$ – $T_r$) during the summer nighttime (Aug 4, 2013) were −0.21 K and 1.13 K respectively, while average and standard deviation on a winter nighttime (Mar 13, 2013) were 0.30 K and 1.13 K respectively.

Specifically, in a high-density built environment, $T_c$ was higher than $T_r$ at night of both Mar 13 and Aug 4, 2013. Lower nighttime $T_r$ then Tc can be explained by heat dissipation at rooftop facets being larger than at wall or street facets. This process of radiative and convective

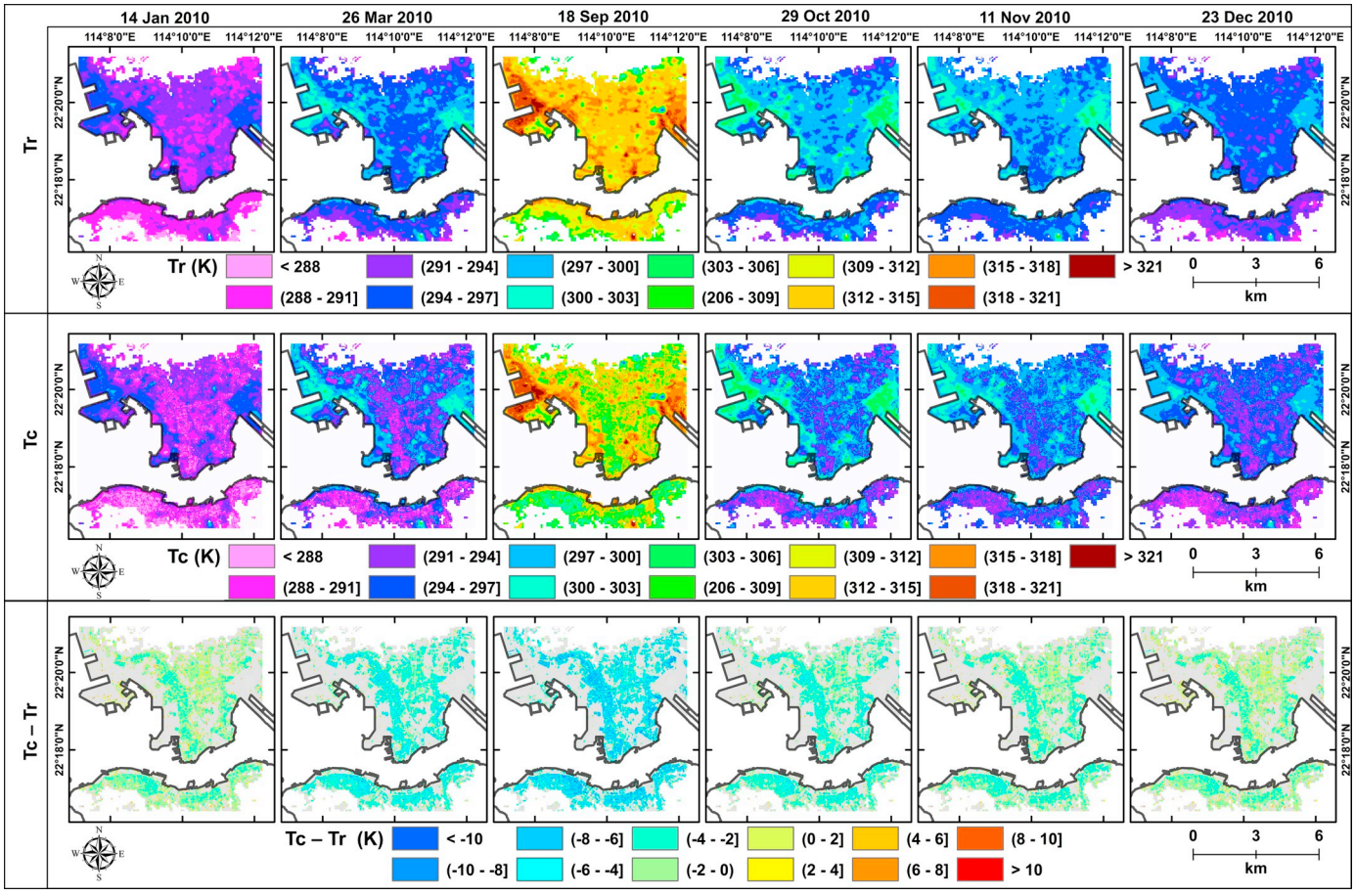



**Fig. 14.** Radiometric, $T_r$, complete, $T_c$, surface temperature and their difference $T_c$ – $T_r$ retrieved from Landsat TM Band 6 in 2010 based on Eq. (8).

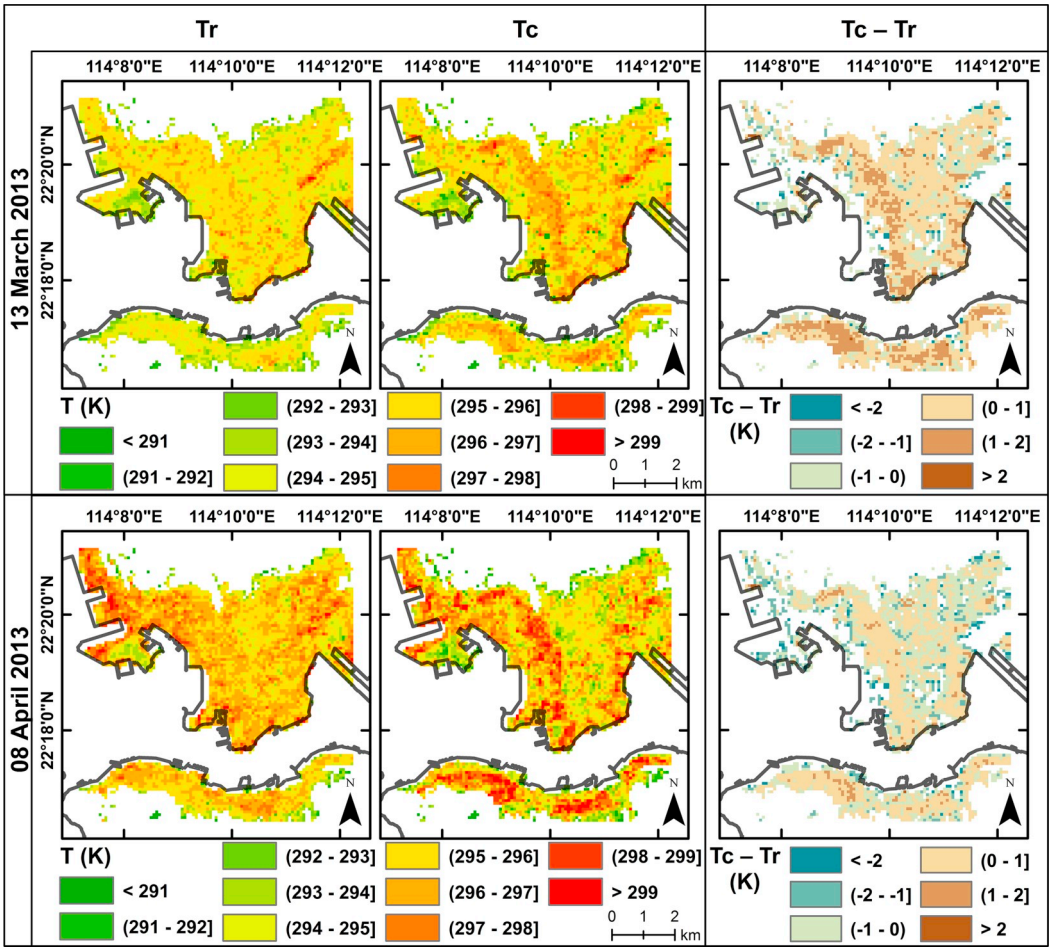



**Fig. 15.** Nighttime $T_r$ and $T_c$ estimated by applying Eq. (9) from ASTER image data and GIS building data in 2013.

**Table 7**
Difference of $T_c - T_r$ between complete and radiometric urban surface temperature in entire images.

| Date | Mean ($T_c - T_r$) (K) | Mean absolute value of ($T_c - T_r$) (K) |
|---|---|---|
| Jan 14, 2010 | −0.861 | 2.133 |
| Mar 26, 2010 | −3.233 | 3.640 |
| Sept 18, 2010 | −4.981 | 5.133 |
| Oct 29, 2010 | −2.442 | 3.00 |
| Nov 30, 2010 | −1.720 | 2.530 |
| Dec 23, 2010 | −0.910 | 2.150 |
| Mar 13, 2013 | 0.310 | 0.784 |
| Aug 4, 2013 | −0.230 | 0.680 |

dissipation is different in daytime, which may result in a lower rooftop surface temperature in the late evening. The latter is likely to determine the $T_r$ observed by a nadir looking TIR imaging radiometer.

Another important factor is daytime heat storage and nighttime heat dissipation by wall facets. The solar elevation angle on Mar 13, 2013 was lower than on August 4, 2013, thus solar irradiance on wall facets was higher in August, and it induced increasing heat storage at wall facets. In addition, building morphology can reduce both radiative and convective cooling of wall facets: wall facet temperature can be higher than rooftop temperature at night. Solar irradiance on wall facets is lower in summer daytime and rooftop temperature decreases rapidly after sunset. This increases the spatial variability of surface temperature during summer daytime, but reduces it during summer nighttime. Thus, the spatial variability of surface temperature at night in summer is smaller than in spring. $T_c$ on August 4, 2013 was lower than $T_r$ in areas with lower building density. This is because the wall facet temperature is lower than the rooftop temperature in some areas at night. In winter, the solar radiation heats up more wall facets within the urban space because of the lower solar elevation angle than in summer. Thus, the wall facet temperature in winter is higher than rooftop temperature, while the wall facet temperature in summer is a little higher than the rooftop temperature.

## 5. Discussion

In this study, the TUF-3D model was used to derive synthetic data on urban climate under different and controlled conditions. The data from TUF-3D model were used to analyze the effects of different urban geometric and climate parameters on the relationship between $T_c$ and $T_r$ in daytime and nighttime. In addition, the numerical experiments showed that the geometric effects on the relationship between $T_c$ and $T_r$ are different at daytime and nighttime. It is difficult to obtain this information based on observational data. This study demonstrates an operational method to estimate $T_c$ from satellite TIR data. The method developed in this study has been validated using the thermal infrared image data at high spatial resolution. In principle, it would be ideal to acquire the high resolution TIR image data simultaneously with either the Landsat TM or ASTER acquisitions for evaluating the estimated $T_c$, but this was not feasible due to practical constraints on the airborne acquisitions. The accuracy of the retrieval of $T_r$ with Landsat TM and ASTER radiometric data is well documented in the literature (Li et al., 2013; Gillespie et al., 1998).

This study only discussed the estimation of $T_c$ from nadir viewed remote sensing thermal data. Jiang et al. (2018) estimated $T_c$ from

airborne thermal data at different view angles and results showed that the observed radiometric temperature is closest to $T_c$ when viewing azimuth and zenith angles are $\theta_a \pm 90^\circ$ and $\theta_z = 45$–$60^\circ$. For off-nadir images, the data can capture information on wall facets, and results show that the observed $T_r$ at off-nadir angles is closer to $T_c$ than the nadir data. Jiang et al. (2018) also indicated that $T_c$ can be improved by measuring directional radiometric temperatures. Currently the SENTINEL-3 SLSTR can provide two-angular thermal images at nadir and forward direction (about 53°), extending the data record collected by the (A)ATSR series instruments (https://sentinel.esa.int/web/sentinel/technical-guides/sentinel-3-slstr/instrument). This may provide an opportunity to estimate the complete surface temperature in the future, albeit at low spatial resolution.

It is difficult to obtain the exact material properties within the mixed pixels. Several studies have shown that geometry is the main determinant of the urban surface temperature distribution (Krayenhoff and Voogt, 2016; Voogt and Oke, 2003), while the material properties still have impact on urban surface temperature distribution. In alternative, this study used the predefined material properties of urban surface models to better evaluate the relationships between $T_c$ and $T_r$ associated with urban materials. This approach may reduce the bias caused by material heterogeneity, while exact information on material properties within a pixel cannot be obtained from satellite images. Sensitivity tests also have been conducted using different typical material properties provided by Stewart et al. (2014), and results showed that the different material properties caused $< 1.5$ °C spread under different geometric and meteorological conditions. This proved that urban geometry has more effect on urban surface temperature distribution than materials. However, we still recommend that the local material properties should be used in further studies.

The TUF-3D can model the radiation and energy flux applying to simple building arrays. Therefore, the complexity of building shape and distributions in real-world, and its associated effects on surface temperature distribution have not been explored. The validation was also carried out over areas without vegetation. In addition, the actual building outlines and structures are not as uniform as in the TUF-3D model. Thus, the simple model developed in this study to estimate the complete urban surface temperature still needs more detailed validation e.g. with in-situ measurements with radiometers or IR-temperature sensor. The solar irradiance and position at a particular location vary across seasons. In this study, the latitude was set as 22.14° N. The relationships between $T_r$ and $T_c$ at different latitudes will be studied further.

We only considered the UST heterogeneity caused by buildings within a pixel, while buildings in neighboring pixels may also influence the spatial variability of temperature by shadowing effect and interference on heat convection. In this study, the highest building is 415.8 m. The shadow of this building may affect adjacent pixels, especially at sunrise and sunset. Thus, our empirical models are more suitable for a city with lower fractional abundance of high-rise buildings.

In this study, the impacts of vegetation cover on temperature were excluded since Hong Kong is an extremely urbanized area. However, vegetation may have a strong effect in some cities with complex interactions, due to the shape and density of vegetation canopy and building morphology. In addition, evapotranspiration of vegetation cover can significantly reduce urban temperatures. Vegetation cover reduces the wind speed and sky view factor. Therefore, further applications using the empirical models developed in this study to other cities may need to require refinements by including the effects of vegetation.

Finally, wind direction was not included in the modelling. Although wind direction is important in urban energy exchange, it is mostly influencing areas with regular orientation of streets and identical city blocks. However, considering that orientation of streets is not regular across Hong Kong (Nichol and Wong, 2005Sobrino, 2007), wind direction may not have a strong effect on UST. For future studies in a city with regularly oriented streets, integration with the relative angle between wind and street orientation may be essential.

## 6. Conclusion

This study explored the relationship between complete urban surface temperature and the nadir radiometric temperature observed from satellites. The relationships between urban geometry and difference between $T_r$ and $T_c$ were developed and results showed that the correlation coefficients are 0.97 for daytime and 0.98 for nighttime, and overall RMSEs are 1.5 °C for daytime and 0.69 °C for nighttime. Daytime relationships between $T_r$ and $T_c$ have been evaluated in this study using higher resolution airborne thermal images and results showed that the correlation coefficients and RMSEs are 0.72, 1.09 °C on August 6, 2013 at 12:40 pm; and 0.86 and 1.86 °C on October 24, 2017 at 11:30 am. The developed relationships were also used to estimate the complete surface temperature from satellite data in Hong Kong. The results showed that daytime difference between $T_c$ and $T_r$ can reach 10 °C in summer and 6 °C in winter, and the difference at night can reach to 2 °C in spring and summer. This study provides a simplified method for estimating complete surface temperature from satellite data, and the multi-angular TIR radiometric data will be used to improve the estimation of urban complete surface temperature in the near future.

## Declaration of competing interest

The authors declare that they have no known competing financial interests or personal relationships that could have appeared to influence the work reported in this paper.

## Acknowledgement

This work was supported in part by the grant of Early Career Scheme (project id: 25201614) from the Research Grants Council, University Grants Committee, the grant 1-ZE24 from the Hong Kong Polytechnic University; and Grants by National Natural Science Foundation of China (41671430, 41901283, 41571366, 61976234, 61601522). The authors thank the Hong Kong Planning Department, Hong Kong Lands Department, the Hong Kong Civil Engineering and Development Department, the Hong Kong Observatory and the Hong Kong Government Flying Service for the planning, building GIS, weather and climate, and airborne Lidar data, and NASA LP DAAC for the Landsat and ASTER satellite imagery. Massimo Menenti acknowledges the support of grant P10-TIC-6114 by the Junta de Andalucía and the SAFEA Long-Term-Projects of the 1000 Talent Plan for High-Level Foreign Experts (grant no. WQ20141100224).

## Appendix A

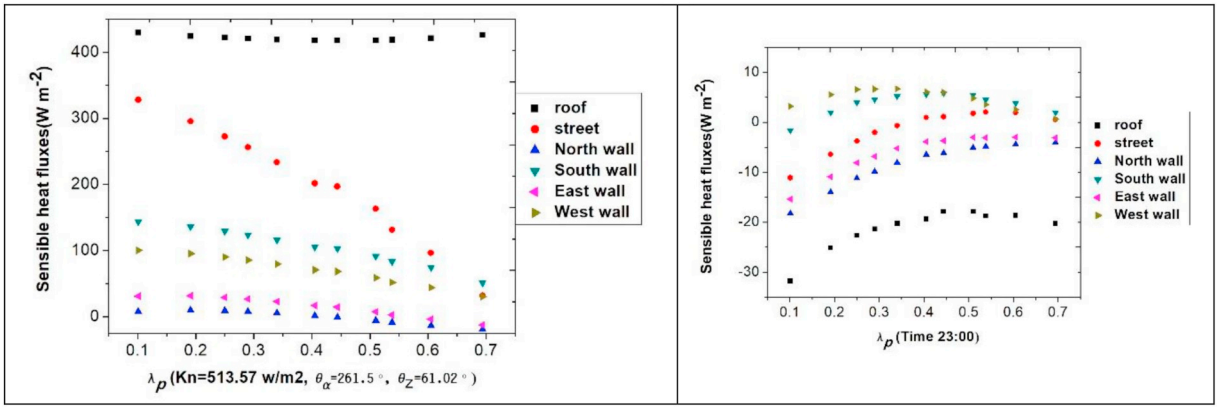



**Fig. 1.** Change of sensible heat fluxes with $\lambda_p$: a daytime; b nighttime.

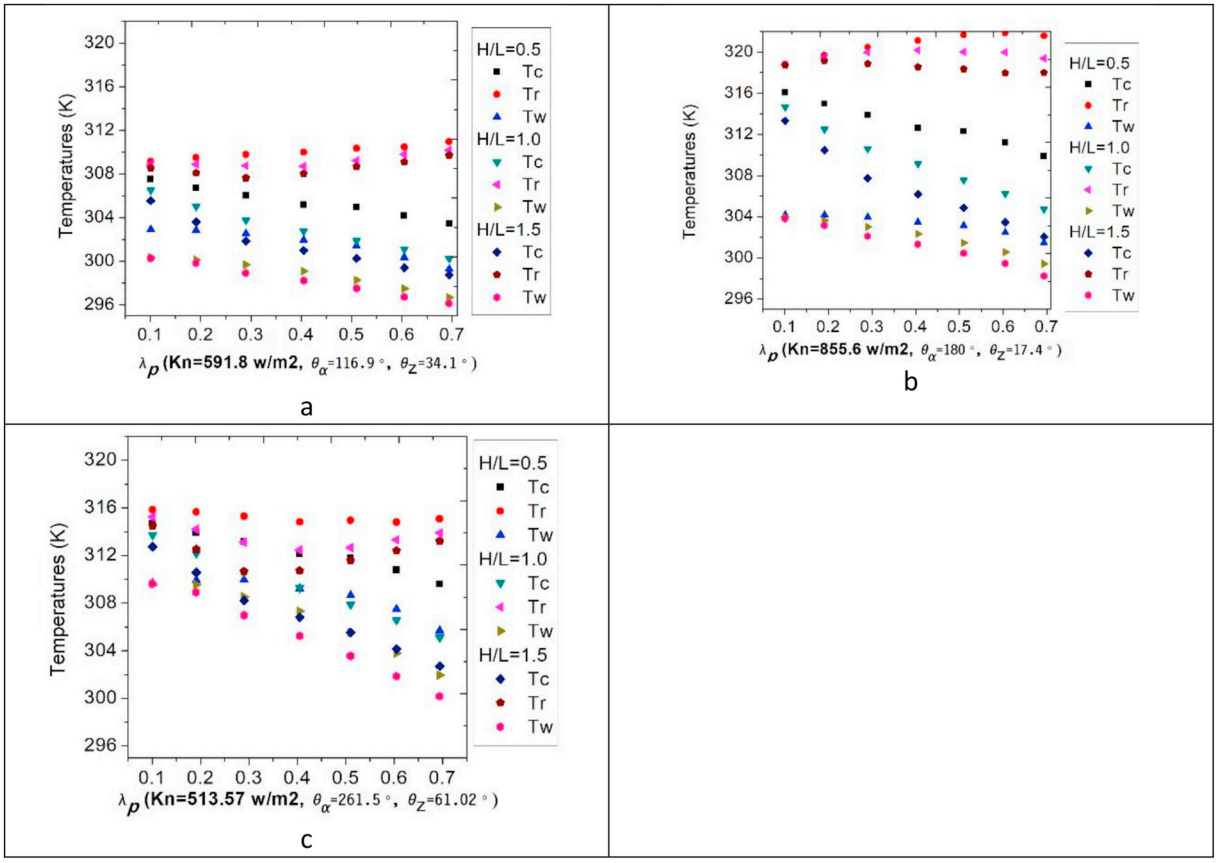



**Fig. 2.** Change of $T_r$ and $T_c$ and $T_w$ (wall surface temperature) with $\lambda_p$.

## References


Adderley, C., Christen, A., Voogt, J.A., 2015. The effect of radiometer placement and view on inferred directional and hemispheric radiometric temperatures of an urban canopy. Atmos. Meas. Tech. 8 (7), 2699–2714.

Ali-Toudert, F., Mayer, H., 2006. Numerical study on the effects of aspect ratio and orientation of an urban street canyon on outdoor thermal comfort in hot and dry climate. Build. Environ. 41 (2), 94–108.

Allen, M., Voogt, J., Christen, A., 2018. Time-continuous hemispherical urban surface temperatures. Remote Sens. 10 (1), 3.

Arnfield, A.J., 2003. Two decades of urban climate research: a review of turbulence, exchanges of energy and water, and the urban heat island. Int. J. Climatol. 23 (1), 1–26.

Arnfield, A.J., Grimmond, C., 1998. An urban canyon energy budget model and its application to urban storage heat flux modeling. Energ. Buildings 27 (1), 61–68.

Becker, F., Li, Z.L., 1995. Surface temperature and emissivity at various scales: definition, measurement and related problems. Remote Sens. Rev. 12 (3–4), 225–253.

Chen, L., et al., 2012. Sky view factor analysis of street canyons and its implications for daytime intra-urban air temperature differentials in high-rise, high-density urban areas of Hong Kong: a GIS-based simulation approach. Int. J. Climatol. 32 (1), 121–136.

Cheng, J., Liang, S., Wang, J., Li, X., 2010. A stepwise refining algorithm of temperature and emissivity separation for hyperspectral thermal infrared data. IEEE Trans. Geosci. Remote Sens. 48 (3), 1588–1597.

Coutts, A.M., Beringer, J., Tapper, N.J., 2007. Impact of increasing urban density on local climate: spatial and temporal variations in the surface energy balance in Melbourne,

Australia. J. Appl. Meteorol. Climatol. 46 (4), 477–493.
Dousset, B., Gourmelon, F., 2003. Satellite multi-sensor data analysis of urban surface temperatures and landcover. ISPRS J. Photogramm. Remote Sens. 58 (1–2), 43–54.
Gillespie, A., et al., 1998. A temperature and emissivity separation algorithm for Advanced Spaceborne Thermal Emission and Reflection Radiometer (ASTER) images. IEEE Trans. Geosci. Remote Sens. 36 (4), 1113–1126.
Grimmond, C., Oke, T.R., 1999. Aerodynamic properties of urban areas derived from analysis of surface form. J. Appl. Meteorol. 38 (9), 1262–1292.
Grimmond, C., et al., 2010. The international urban energy balance models comparison project: first results from phase 1. J. Appl. Meteorol. Climatol. 49 (6), 1268–1292.
Grimmond, C., et al., 2011. Initial results from Phase 2 of the international urban energy balance model comparison. Int. J. Climatol. 31 (2), 244–272.
Jiang, L., et al., 2018. Remote estimation of complete urban surface temperature using only directional radiometric temperatures. Build. Environ. 135, 224–236.
Kanda, M., et al., 2005. A simple energy balance model for regular building arrays. Bound.-Layer Meteorol. 116 (3), 423–443.
Kanda, M., Kanega, M., Kawai, T., Moriwaki, R., Sugawara, H., 2007. Roughness lengths for momentum and heat derived from outdoor urban scale models. J. Appl. Meteorol. Climatol. 46 (7), 1067–1079.
Kastendeuch, P.P., Najjar, G., 2009. Simulation and validation of radiative transfers in urbanised areas. Sol. Energy 83 (3), 333–341.
Kastendeuch, P.P., Najjar, G., Colin, J., 2017. Thermo-radiative simulation of an urban district with LASER/F. Urban Clim. 21, 43–65.
Krayenhoff, E.S., Voogt, J., 2007. A microscale three-dimensional urban energy balance model for studying surface temperatures. Bound.-Layer Meteorol. 123 (3), 433–461.
Krayenhoff, E.S., Voogt, J.A., 2016. Daytime thermal anisotropy of urban neighbourhoods: morphological causation. Remote Sens. 8 (2), 108.
Kotthaus, S., Smith, T.E.L., Wooster, M.J., Grimmond, C.S.B., 2014. Derivation of an urban materials spectral library through emittance and reflectance spectroscopy. ISPRS Journal of Photogrammetry and Remote Sensing 94, 194–212.
Krayenhoff, E.S., Christen, A., Martilli, A., Oke, T.R., 2014. A multi-layer radiation model for urban neighbourhoods with trees. Bound.-Layer Meteorol. 151 (1), 139–178.
Kusaka, H., Kimura, F., 2004. Thermal effects of urban canyon structure on the nocturnal heat island: numerical experiment using a mesoscale model coupled with an urban canopy model. J. Appl. Meteorol. 43 (12), 1899–1910.
Lai, A., So, A.C., Ng, S., Jonas, D., 2012. The territory-wide airborne light detection and ranging survey for the Hong Kong Special Administrative Region. In: The 33RD Asian Conference on Remote Sensing, pp. 26–30.
Lee, D., et al., 2013. Modeling and Observation of Heat Losses From Buildings: The Impact of Geometric Detail on 3D Heat Flux Modeling.
Lemonsu, A., Grimmond, C.S.B., Masson, V., 2004. Modeling the surface energy balance of the core of an old Mediterranean city: Marseille. J. Appl. Meteorol. 43 (2), 312–327.
Li, Z.-L., et al., 2013. Satellite-derived land surface temperature: current status and perspectives. Remote Sens. Environ. 131, 14–37.
Martilli, A., Clappier, A., Rotach, M.W., 2002. An urban surface exchange parameterisation for mesoscale models. Bound.-Layer Meteorol. 104 (2), 261–304.
Morrison, W., et al., 2018. A novel method to obtain three-dimensional urban surface temperature from ground-based thermography. Remote Sens. Environ. 215, 268–283.
Nazarian, N., Kleissl, J., 2015. CFD simulation of an idealized urban environment: thermal effects of geometrical characteristics and surface materials. Urban Clim. 12 (0), 141–159.
Nazarian, N., Fan, J., Sin, T., Norford, L., Kleissl, J., 2017. Predicting outdoor thermal comfort in urban environments: a 3D numerical model for standard effective temperature. Urban Clim. 20, 251–267.
Nazarian, N., Martilli, A., Kleissl, J., 2018a. Impacts of realistic urban heating, part I: spatial variability of mean flow, turbulent exchange and pollutant dispersion. Bound.-Layer Meteorol. 166 (3), 367–393.
Nazarian, N., Martilli, A., Norford, L., Kleissl, J., 2018. Impacts of realistic urban heating. Part II: air quality and city breathability. Bound.-Layer Meteorol. 168, 321–341.
Nichol, J., Wong, M.S., 2005. Modeling urban environmental quality in a tropical city. Landscape and Urban Planning 73, 49–58.
Oke, T., 1988. The urban energy balance. Prog. Phys. Geogr. 12 (4), 471–508.
Peng, F., Wong, M.S., Ho, H.C., Nichol, J., Chan, P.W., 2017. Reconstruction of historical datasets for analyzing spatiotemporal influence of built environment on urban microclimates across a compact city. Build. Environ. 123, 649–660.
Roth, M., Oke, T.R., Emery, W.J., 1989. Satellite-derived urban heat islands from three coastal cities and the utilization of such data in urban climatology. Int. J. Remote Sens. 10 (11), 1699–1720.
Sobrino, J.A., et al., 2007. Accuracy of ASTER Level-2 thermal-infrared Standard Products of an agricultural area in Spain. Remote Sensing of Environment 106, 146–153.
Stewart, I.D., Oke, T.R., Krayenhoff, E.S., 2014. Evaluation of the 'local climate zone' scheme using temperature observations and model simulations. Int. J. Climatol. 34 (4), 1062–1080.
Voogt, J.A., Oke, T.R., 1997. Complete urban surface temperatures. J. Appl. Meteorol. 36 (9), 1117–1132.
Voogt, J.A., Oke, T.R., 2003. Thermal remote sensing of urban climates. Remote Sens. Environ. 86 (3), 370–384.
Wang, L., et al., 2014. Turbulent transport of momentum and scalars above an urban canopy. Bound.-Layer Meteorol. 150 (3), 485–511.
Weng, Q., 2009. Thermal infrared remote sensing for urban climate and environmental studies: methods, applications, and trends. ISPRS J. Photogramm. Remote Sens. 64 (4), 335–344.
Yaghoobian, N., Kleissl, J., Krayenhoff, E.S., 2010. Modeling the thermal effects of artificial turf on the urban environment. J. Appl. Meteorol. Climatol. 49 (3), 332–345.
Yang, X., Li, Y., 2015. The impact of building density and building height heterogeneity on average urban albedo and street surface temperature. Build. Environ. 90 (0), 146–156.
Yang, J., et al., 2016. Development of an improved urban emissivity model based on sky view factor for retrieving effective emissivity and surface temperature over urban areas. ISPRS J. Photogramm. Remote Sens. 122, 30–40.